5-22-2006

# Complex Crustal Stratification Within the Chugach Mountains, Southern Alaska

Leland O'Driscoll
*University of New Orleans*

# COMPLEX CRUSTAL STRATIFICATION WITHIN THE CHUGACH MOUNTAINS, SOUTHERN ALASKA

A Thesis

Submitted to the Graduate Faculty of the
University of New Orleans
in partial fulfillment of the
requirements for the degree of

Master of Science
in
Geology and Geophysics

by

Leland O'Driscoll

B.A. Humboldt State University, 2003

May, 2006

## Table of Contents

## List of Figures

**Abstract**

Strain within the crust is accommodated along vertical gradients, but a general characterization is difficult given the heterogeneity of the earth's outermost layer. The western termination of the Chugach metamorphic complex in southern Alaska includes a uniquely well exposed crustal section ideal for obtaining the vertical profile of a crustal section. Field studies in this area resulted in the characterization of deformational fabric and analysis of finite strain magnitude and orientation. These observational data provide constraints for kinematic modeling following results presented in Teyssier and Cruz (2004). By optimizing the fit between field data, finite strain analysis, and modeling, a complex ductile stratification of the crust is inferred. I conclude that strain was concentrated within the lower crust, becoming more diffuse in upper ductile levels. This unconventional crustal stratification and vertical strain gradient was consistent with an anomalously high thermal gradient created by the adjacent subducting spreading ridge.

## Introduction

The vertical distribution of strain throughout the crust is not well understood in strike slip regions, particularly below the brittle-ductile transition. Few exposures of complete crustal sections have been described, and rheology, pressure, and temperature gradients make these exposures difficult to interpret. This study contributes to the resolution of the problem of crustal strain distribution, specifically within a mid-crustal transition of a strike-slip system.

The Chugach Mountains in southern Alaska (Figure 1) provide an excellent setting to investigate deformation through numerous crustal levels. The northern Cordilleran margin has a long-lived history of convergence, uplift, erosion/exhumation, and transpressive/transtensional behavior (e.g. Plafker et al., 1994; Nokleberg et al., 1994; Bradley et al., 2003). During the history of the plate margin, triple junction interactions led to a series of complicated oblique and compressional geologic events that overprinted long-lived subduction zone processes (e.g. Sisson and Pavlis, 1993; Bradley et al., 2003). For example, the subduction of a spreading ridge a left signature of a high thermal gradient recorded by low P-high T (650 C) metamorphic assemblages in the Chugach metamorphic complex (Sisson et al., 1989). The high temperature event recorded by the Chugach metamorphic complex (CMC) provides an exceptional setting for investigating the properties of ductile deformation.

The research described in this paper focuses on ductile deformation adjacent to the western termination of the CMC. After presenting the results of mapping and finite strain data, a model is presented that explains the observed deformation pattern. The success of this approach is examined, illustrating

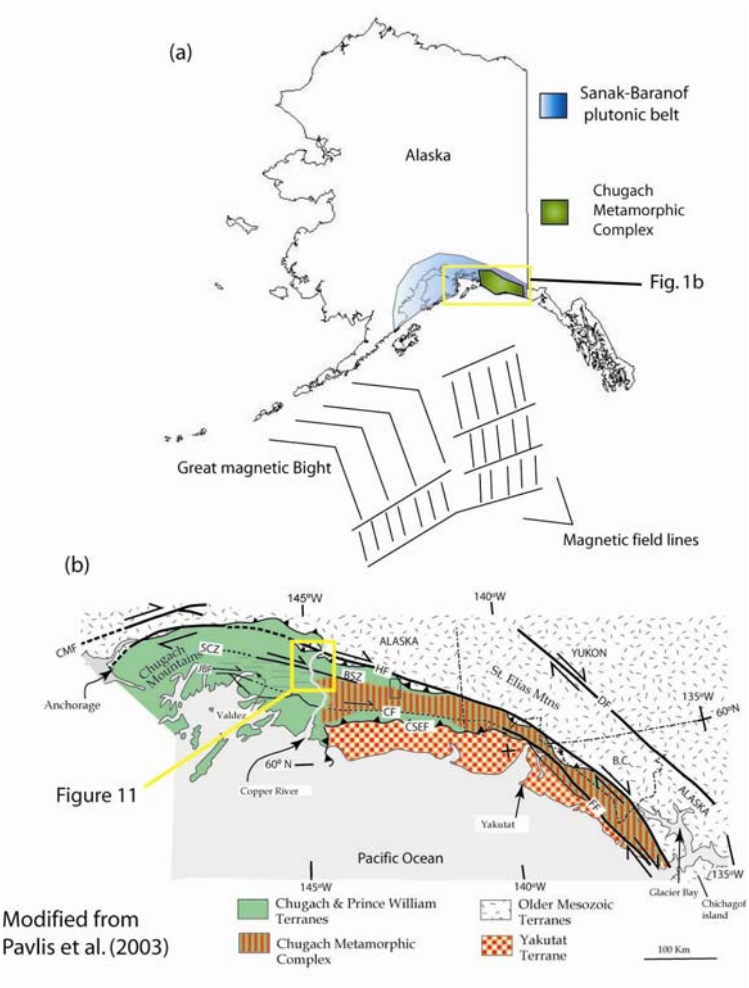


Figure 1. Regional setting of field area. (a) Geologic elements providing evidence of spreading ridge subduction along the southern Alaskan margin. The Sanak-Baranof plutonic belt marks the location of igneous activity within Paleogene accretionary prism rocks. See text for description of other features. (b) Location of the Chugach metamorphic complex. Vertical bars show extent of the high T, low P metamorphic belt that affected the Cretaceous Valdez group accretionary prism rock (green). The extent of the field area studied in this thesis is indicated in the yellow box.

compatibility amongst these lines of evidence, as well as the possibility for alternative explanations that explain the field relationships.

## Background

### Tectonic Setting

The northeast Pacific margin provides the regional geology that is the basis of the Baja British Columbia hypothesis (Umhoefer, 1987; Cowan and Brandon, 1981). Many “suspect terranes” are thought to have traveled as many as thousands of kilometers northward along the northern Cordilleran margin since the Mesozoic through combinations of subduction and strike-slip. The Chugach terrane in southern Alaska

provides an excellent example of one of the northward-translating blocks of Baja B.C (Bol, 1993). Along with large-scale terrane motion, the northern Cordillera has experienced complex plate interactions and reorganizations. Atwater (1970) provided early observations that identified this complex history on the basis of sea floor spreading anomalies. The Great Magnetic Bight in the Gulf of Alaska provides evidence of a past triple junction, indicated by a complex pattern of magnetic chrons in the oceanic crust. While arguing for ridge subduction, Bradley et al. (2003) state, “if the Great Magnetic Bight is the smoking gun, then the Sanak Baranof plutonic bodies are the bullet holes.” This comment refers to the relationship between the observation of magnetic stripes on the seafloor and high-temperature plutonic activity (Figure 1a). Both the magnetic anomalies and plutonic activity provide evidence that support the presence of a trench-ridge-trench triple junction along the Paleogene margin in southern Alaska and northern Canada.

The research presented in this paper is based on field and modeling results intended to analyze deformation that occurred within the Chugach terrane. This terrane is a fragment of a Cretaceous-Eocene accretionary prism that was generated along the Northern Cordilleran plate margin (e.g. Sisson and Pavlis, 1993; Pavlis and Sisson, 1995). Subsequently, the Chugach terrane was translated northward as a forearc sliver (Pavlis and Sisson, 1995, figure 1). Figure 1b shows the regional geologic setting of the Chugach terrane that is bounded to the north (present day coordinates) by the Border Ranges/Hanagita Fault and to the south by the Chugach-St. Elias fault.

Lithology

The Chugach terrane is composed primarily of rocks in the Valdez Group with subordinate older mélange assemblages along the inboard edge of the terrane. The bulk of the Chugach terrane consists of Cretaceous accretionary prism although the mélange assemblages may comprise older Mesozoic subduction (Plafker et al., 1994). Argillites, fine-grained sandstones, and conglomerates are the dominant lithology of the Valdez Group (Nilsen and Zuffa, 1982). Locally, thin-bedded limestone and volcanic tuff are present. The Valdez Group is the lateral equivalent of the Kodiak Formation that is named for the type section on Kodiak Island, Alaska.

The Valdez Group is structurally overlain by the McHugh complex, a mélange consisting of pervasively deformed volcanic tuff, limestone, argillite, and sandstone. The contact between these units is a major, typically low-angle, fault that is generally referred to as the Eagle River fault in the Chugach Mountains (e.g. Clark, 1981). Structurally beneath the Valdez Group is the Orca Group, an accretionary prism assemblage that is in part coeval with the Valdez Group (Farmer et al., 1993) but also contains younger sedimentary and volcanic rocks as young as Eocene (Plafker et al., 1994). Most of the Orca Group is a coherent assemblage like the Valdez Group, but locally consists of a stratally disrupted mélange (Plafker et al., 1994). The Orca Group is distinguished regionally as the “Prince William Terrane” and its contact with the Valdez Group is called the Contact fault. Figure 2 summarizes the relative stratigraphic position of these units.

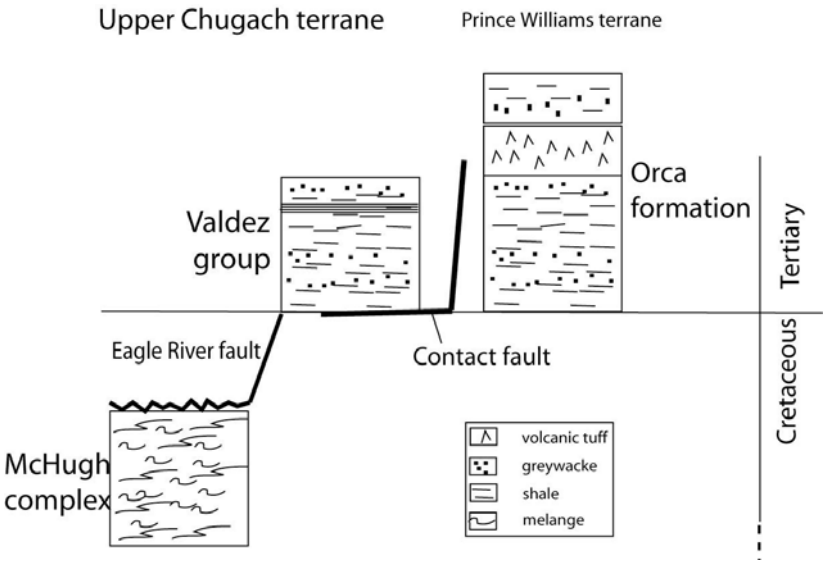


Figure 2. Schematic stratigraphic column of lithologic units in this study divided into terranes. Bold lines indicate fault contacts.

Within the study area, the CMC is derived exclusively from the Valdez Group, although immediately to the south Orca Group rocks were involved in CMC metamorphism (e.g. Pavlis and Sisson, 2003). A range of metamorphic facies are observed in the Valdez group to produce rocks that are described in the next subsection. In addition, the CMC is intruded by numerous generations of plutonic bodies. Granodiorite, tonalite, and trondhjemite intrusions show geochemical evidence of a mixed magmatic source containing MORB and anatectic melts of the Chugach metamorphic assembly, a relatively clear signature of ridge subduction (Harris et al., 1996). Dating of these rocks provides important age constraints on the deformation and metamorphism (Sisson et al., 1989; 2003).

Metamorphism

Two phases of metamorphism took place within the Valdez Group. During initial development as an accretionary prism, lower greenschist to sub-greenschist facies developed synchronously with the formation of a thrust-imbricate fabric (Sample and

Fischer, 1986). However, metamorphism responsible for the creation of the CMC is of much greater importance to this study. Described in Sisson et al. (1989), the CMC underwent upper amphibolite conditions during a high-T (650° C), low-P (3 kbar) event. These conditions are strongly linked to the subduction of a spreading ridge and subsequent formation of a slab window (Sisson et al., 1989, 2003). A garnet-cordierite-sillimanite mineral assemblage within gneiss characterizes the core of the CMC (Sisson et al., 1989). Sillimanite rims surround andalusite cores and in boudinaged andalusite pseudomorphs (figure 3), providing evidence of prograde metamorphism that peaked during the last (D3) phase of deformation (Pavlis and Sisson, 1995, 2003; Sisson et al., 2003).

A lower grade envelope of schist and phyllite surrounds the high-grade core of the metamorphic complex. The schist is characterized by andalusite, biotite, and chlorite with increasing distance from the gneissic core, spanning the high-T greenschist field, whereas the phyllite exhibits lower greenschist (biotite zone) to sub-greenschist metamorphism. These zones of decreasing metamorphic grade are an important part of this study because they provide the key evidence that the area exposes an oblique crustal section exposing various structural levels within a thermally stratified crust.

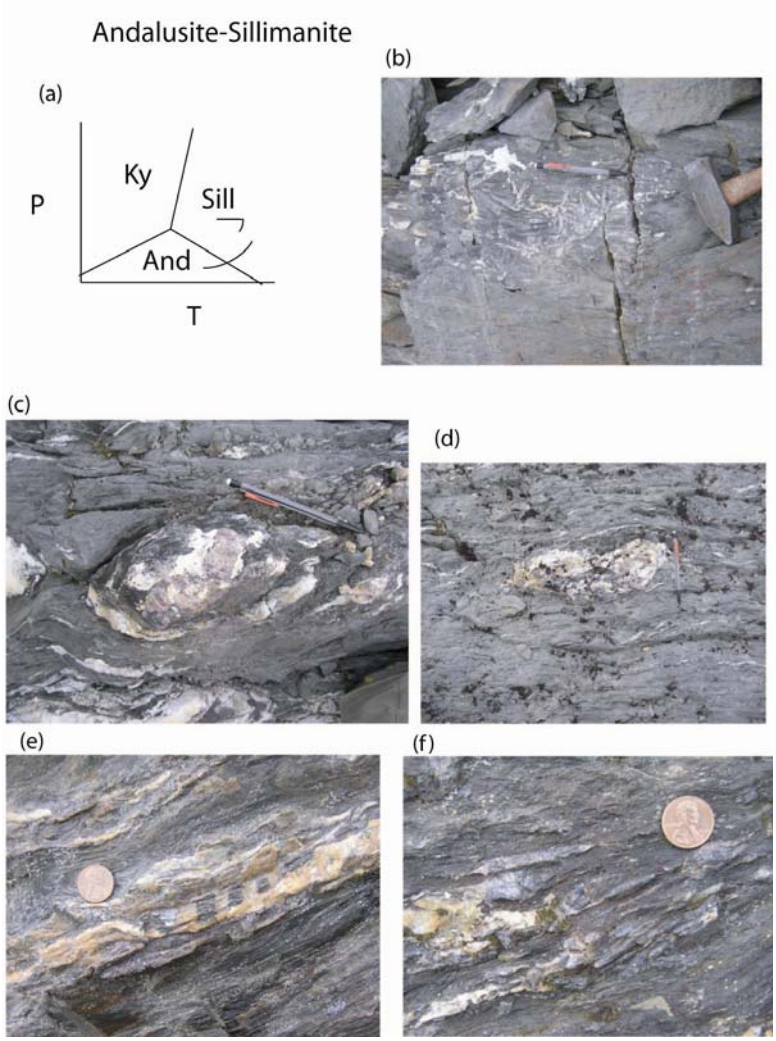


Figure 3. Photographs of aluminosilicate minerals indicative of CMC metamorphism. (f) zoned mineralogy indicating prograde metamorphism; andalusite core surrounded by sillimanite exterior shows crystallization history sketched on the pressure-temperature diagram

**Previous Structural Work**

Pavlis and Sisson (1995, 2003) presented a multi-phase structural history along the northern margin of the CMC in the Tana River area. A three-phase deformation history is described to have taken place during an 8 m.y. time interval. The first deformation fabric, $D_1$, is attributed to shortening and imbrication during subduction zone convergence. The subsequent fabrics were shown to be nearly synchronous with prograde metamorphism that was responsible for the formation of the CMC. $D_2$ fabric is attributed to orogen-parallel extension and vertical shortening temporally close to the

subduction of the Kula-Farallon spreading ridge. $D_3$ followed shortly after, during the metamorphic peak, marking a return to subhorizontal contraction associated with dextral oblique subduction. Each of these phases is linked to a series of melt injections, providing excellent age constraints on this dynamic series of deformational events.

The structural framework described above is used for the structural history at the western termination of the CMC. Pavlis and Sisson (2003) extended the three-part deformation history to the Copper River area, where the high-grade core of the Chugach Metamorphic Complex plunges beneath lower grade crust. The work presented in this paper describes a sub-horizontal decoupling horizon based on the variation of structural fabrics amongst crustal levels.

The gneissic core of the CMC displays a pervasive vertical fabric ($S_3$), indicated by ubiquitous horizontal to gently plunging, upright close to isoclinal folds in S2 foliation and compositional layering. In contrast, the structurally higher schist records a variable fabric with variations in intensity of D2 and D3 fabrics, and variable dip domains from areas of steep foliation and upright folds to flat fabrics with open to sub-isoclinal recumbent folds. The structural fabric distinction between the schist and gneiss is the main line of evidence Pavlis and Sisson (2003) used to interpret the western termination of the CMC as a sub-horizontal decoupling horizon. This study tests this hypothesis by kinematically modeling this stratification scheme.

Other significant structural features are present in the study area. Major $D_3$ shear zone structures such as the Bremner shear zone and Wernicke Glacier shear zone show a strong vertical fabric in the schist, but appear to diffuse into the gneissic core

with deepening structural level. Structural generation assignments for all the features described above are identical to those of Pavlis and Sisson (1995).

This characterization of structural domains provides evidence for a deformation horizon above the gneiss. Combined with the vertical shear zones that trend into this transition, the decoupling surface inspired my research. In the following sections, an application of a decoupling model is described with the intention of reproducing map observations from the area that surrounds the northwest termination of the CMC.

## Methods

The methodology of this study consists of three major components: field mapping, finite strain analysis, and kinematic numerical modeling.

### Field Mapping

Fieldwork was conducted by foot traverse from helicopter established base camps. Eleven, 4 to 5 day camps were completed during the summers of 2003 and 2004. Fieldwork consisted of structural mapping of surfaces and lines.

Mapping was conducted using the program *ArcPad* on *Ipaq* handheld computers. Georeferenced digital maps provided a base layer with GPS located mapping stations overlain. Planar surfaces were mapped as lines representing the intersection of structural elements such as foliation, axial plane surfaces, and bedding (Figure 4) with topography. Mapped data also included linear elements such as extension lineations, intersection lineations, fold axes, and deformed veins and clasts.

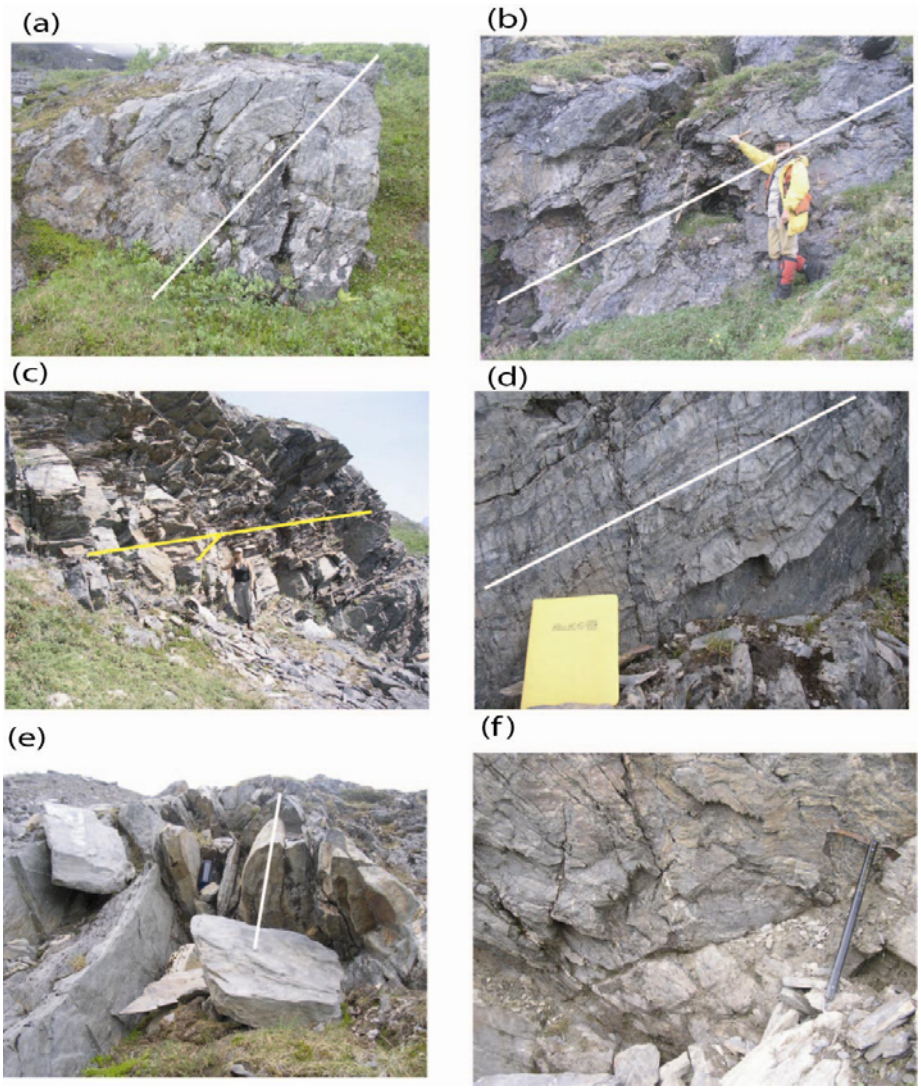


Figure 4. Photographs of representative rock fabrics. White lines indicate the trace of axial plane cleavages, including flat to steep orientations. Yellow line in (c) indicates strike of foliation. (f) Original bedding, S0=S1, folded twice.

Figure 5 shows foliation and lineation data collected in 2004. These data provide a representative summary of structures from entire camps. Note the parallel relationship between lineation direction and strike of all foliation data.

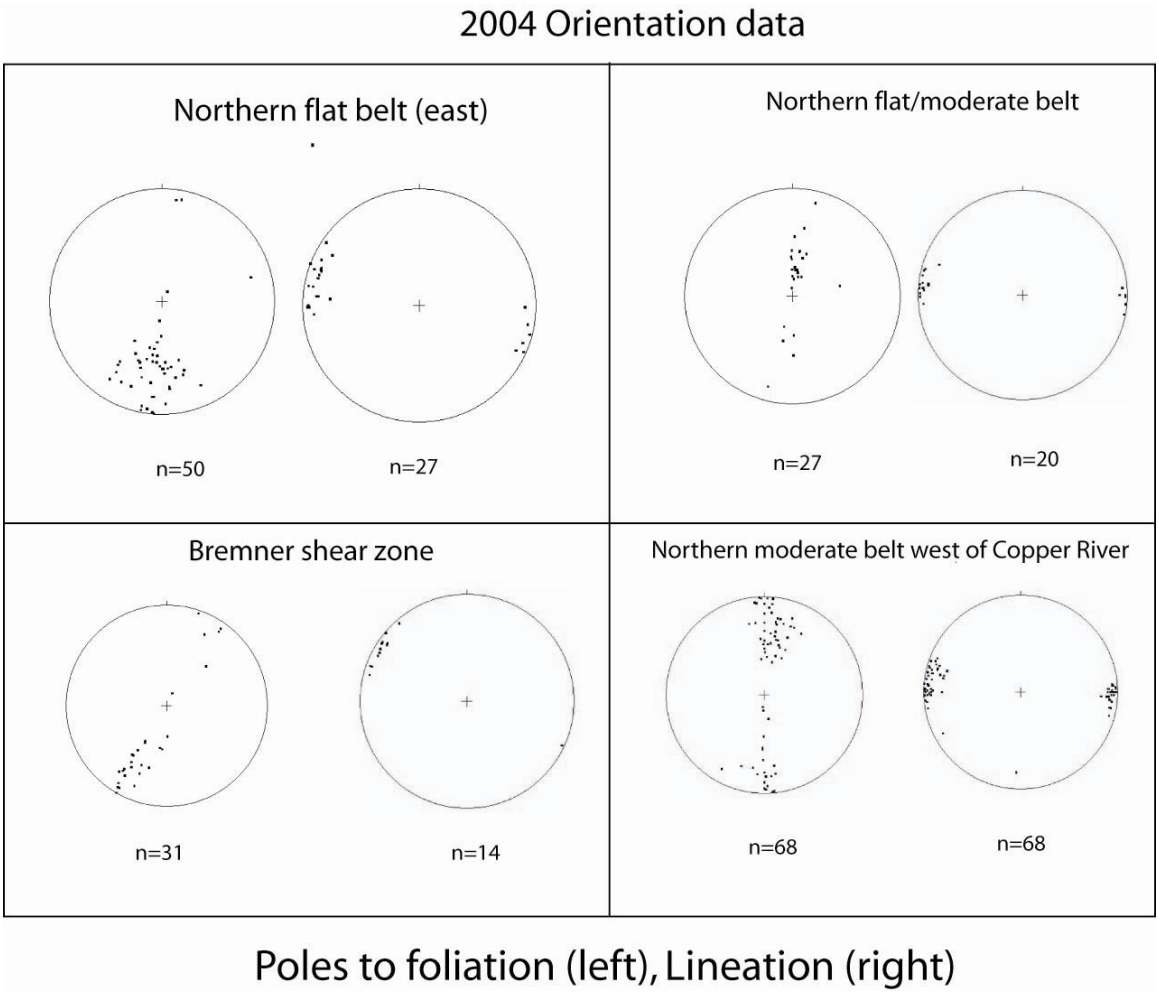


Figure 5. Orientation data from defined zones of continuous foliation orientation indicated in foliation map (figure 11).

Lithologic observations focused on metamorphic facies and mineral assemblages. This aspect of mapping was limited by the monotony of the Valdez Group lithology, although care was taken to distinguish sandstones from argillite.

Finite Strain Analysis

Another approach to developing a quantitative understanding of the deformation history was to use finite strain analysis of deformed clasts and sand grains. Samples were collected containing meso-macroscopic sediments within microscopic matrix.

Figure 6 & 7 provides images from each step of the process described below. Each sample was cut into three mutually perpendicular sections. A 10X magnification photomicrograph was taken from each section and imported into *Adobe Illustrator*. Grain outlines were drawn by hand (minimum of 100 when possible), where interpretation was included in this step because of the presence of growth fibers in grain outlines (Figure 6). These outlines were exported to *Scion Image* (*Windows* version of *NIH Image*, Meyers Instruments and Scion Corporation) for analysis of ellipsoidal properties. This image analysis program used the grain boundaries to calculate grain area, grain center, ellipse axes, angle of long axis of ellipse, and numerous other characteristics. For each thin section and corresponding ellipse properties, $R_f$ vs. Phi analysis was conducted to obtain a value for strain magnitude and orientation within the section. These strain values and orientations for the 3 perpendicular sections were entered into the program *3Dstrain* program provided by Adolf Yonkee. This 3D program calculated an ellipsoid for the sample, yielding lineation, foliation, and stretching magnitude (Figure 7). Results from this analysis are presented in the next section.

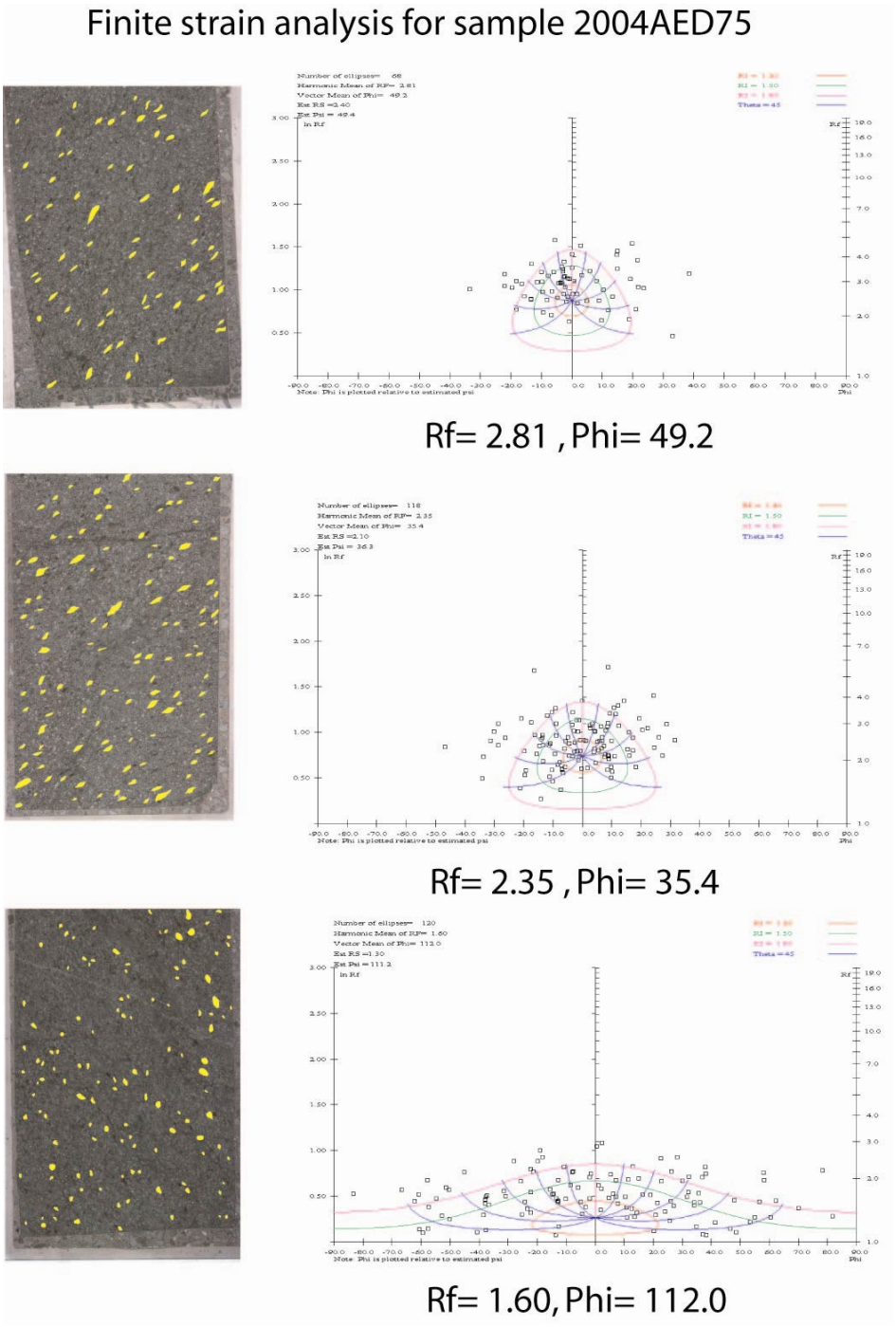


Figure 6. First two steps of determining 3D finite strain. (left) Overlay of grain outlines on photomicrographs from mutually perpendicular sections of sample 2004 AED75. (right) Rf vs. phi plot taken from data from analysis of elliptical properties. Each 2D section yields a single strain ellipse and orientation.

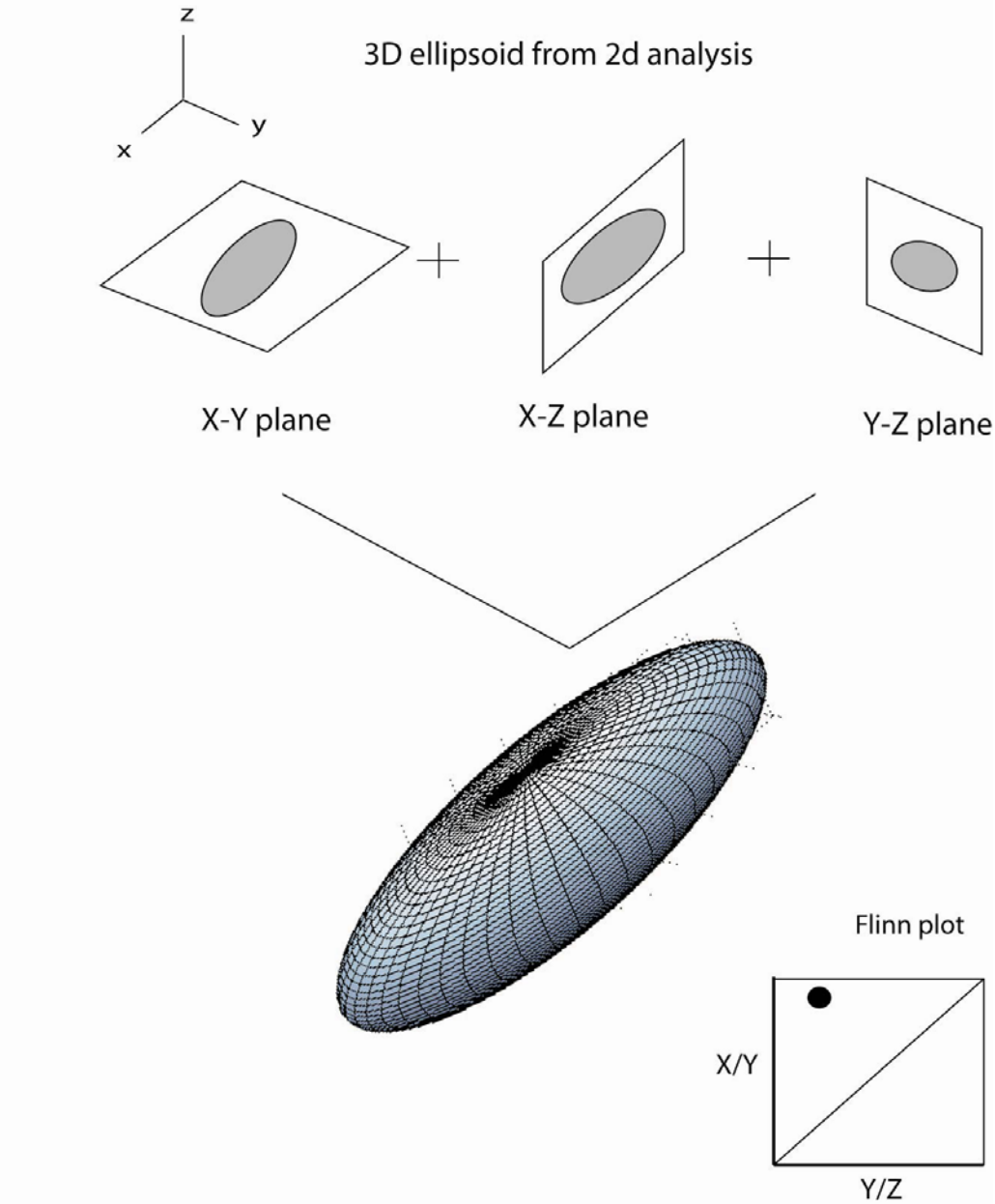


Figure 7. Schematic of the calculation of a 3D ellipsoid from the 2D data illustrated in figure 6. The program *3d-strain* calculates a best-fist ellipsoid from the 3 sections cut in each finite strain sample.

Modeling

Following the attachment zone model of Teyssier et al. (2002) and Teyssier and Cruz (2004), an attachment zone program was developed using Matlab. This forward kinematic model calculates finite strain magnitudes and orientations and outputs a cross section that predicts the foliation and lineation pattern of a crustal layer between two layers that undergo differential displacement. This intervening crustal layer is termed an "attachment zone" by Teyssier et al. (2002). This layer is broken into horizontal and vertical intervals (Figure 8a), where each block is a homogeneous 3D body for which a finite strain ellipsoid is calculated after applying various strains. Three input strain values are established that are estimated from a displacement model (Figure 9). Two strains are simple shear strains on perpendicular planes, and the third strain is a pure shear. Figure 8b shows a cross sectional view of the horizontal shear strains ($\gamma_{HS}$, left) and a map view of the wrench strains ($\gamma_W$). Simple shear occurs as the boundary layers deform along a fault/shear zone in one layer, and through homogeneous shear within the other layer (Figure 8b).

Figure 9a shows a map view of the two boundary layers with open and closed arrows indicating the position of maximum and minimum horizontal simple shear strain, respectively. This diagram represents the displacement model mentioned above. Maximum strain values are located where the greatest relative motion between the upper and lower boundary layers occurs, whereas minimum strain values arise from points where there is no differential motion between layers; a linear gradient between maxima and minima completes the

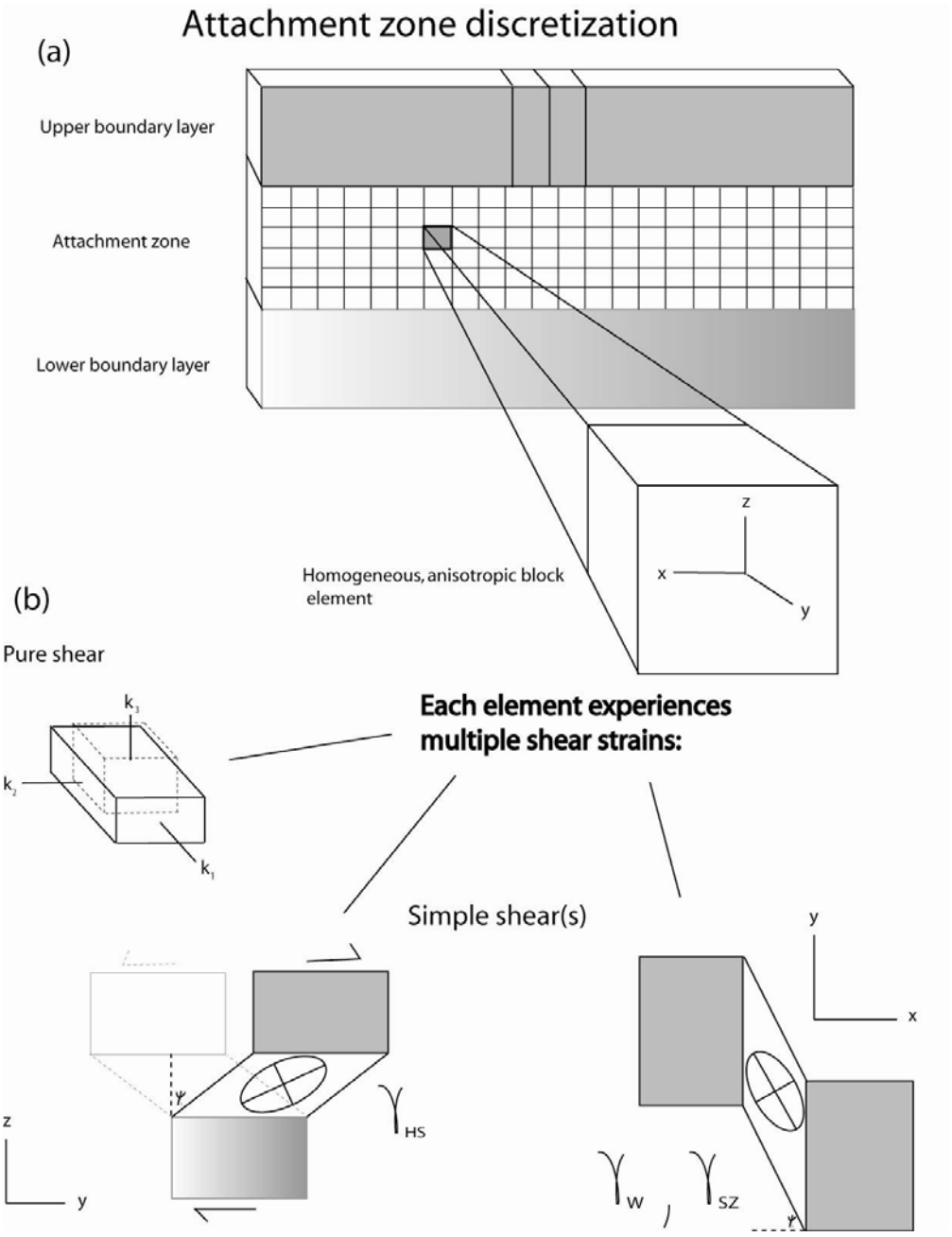


Figure 8. Discretization of the attachment zone model and a summary of the strains imposed on each block. (a) Illustration of the position of the attachment zone between two boundary layers. (b) For each of the discretized blocks in the model, pure shear and two orthogonally oriented simple shears are imposed. For each type of simple shear, note the axes provided in each view and the symbol given to each shear value.

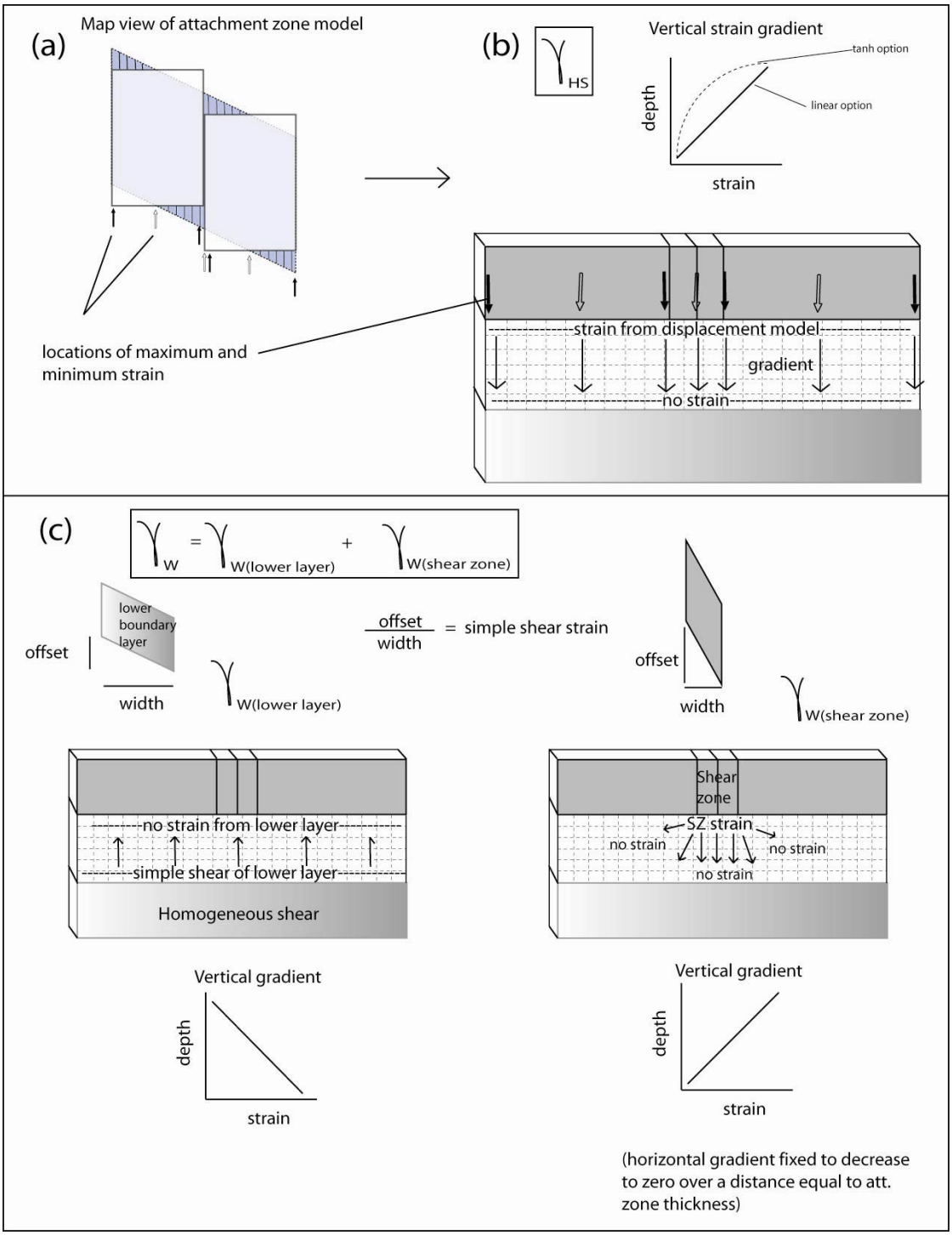


Figure 9. Illustration of strain model that determines prescribed strain values that affect each model block. (a) map view of boundary layers showing position of maximum and minimum differential offset. These values determine an across-strike simple shear strain profile. (b) Vertical distribution of the across-strike profile into the attachment zone; after imposing this gradient, each block in the attachment zone has a unique gammaHS value. (c ) Contributions of wrench stain into the attachment zone. (left) Simple shear in the lower boundary layer is distributed upward through the att zone. (right) Shear within the upper layer shear zone is distributed downward and laterally into the att zone.

displacement model. Figure 9b shows how the horizontal strain distribution described above is dispersed vertically (decreasing with depth) into the attachment zone.

Similarly, in figure 9c, wrench strains associated with the lower boundary layer (left) and upper layer shear zone (right) are dispersed into the attachment zone. Because the two wrench strains have identical spatial orientation, the values are added together when building the deformation matrix used to calculate a strain ellipsoid for each element (see below).

A unique set of the strain values mentioned above are defined for each element in the attachment zone using the described gradients. Once a full array of strain values for each element is determined, they fill a deformation matrix (Tikoff and Fossen, 1993; Fossen and Tikoff, 1993). Once constructed, the eigenvalues and eigenvectors of the matrix are determined from the components of the corresponding strain tensor (Figure 10). The strain tensor components yield values for lineation, foliation, and finite strain magnitude. These modeled quantities are identical to those determined in the finite strain analysis. Once these structural values are solved for, the attachment zone cross section can be built.

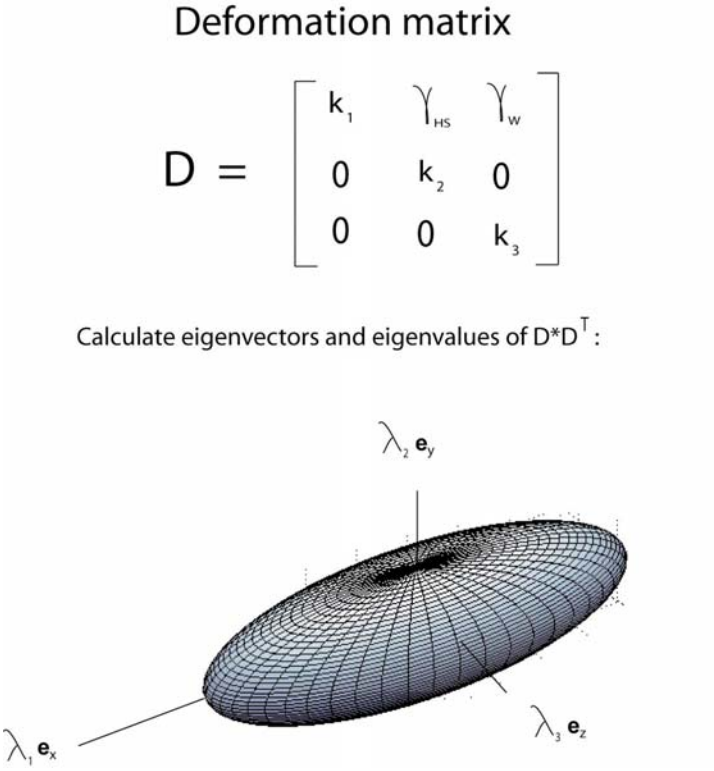


Figure 10. Deformation matrix. All strain values shown in figures 8 and 9 are placed into a strain matrix. Following the method of Tikoff and Fossen (1993), the magnitude and orientation of the three principal axes are calculated for each element in the attachment zone.

**Results**

Field observations

Figure 11 is a representative foliation map resulting from field traverses and helicopter-assisted reconnaissance. The foliation pattern is broken into three categories: vertical to sub-vertical (red), moderate dip (blue), sub-horizontal (gold). These units do not distinguish generational relationships, but aside from the Bremner shear zone features, which are S3 foliation traces, the main foliation outside the gneissic core is S2 in the terminology of Pavlis and Sisson (1995). That is, the foliation is comprises the main continuous cleavage that overprints an earlier layer-parallel phyllitic cleavage.

The most pronounced feature of the mapped area is a large vertical foliation band following the trace of the Bremner River. Figure 12 shows this

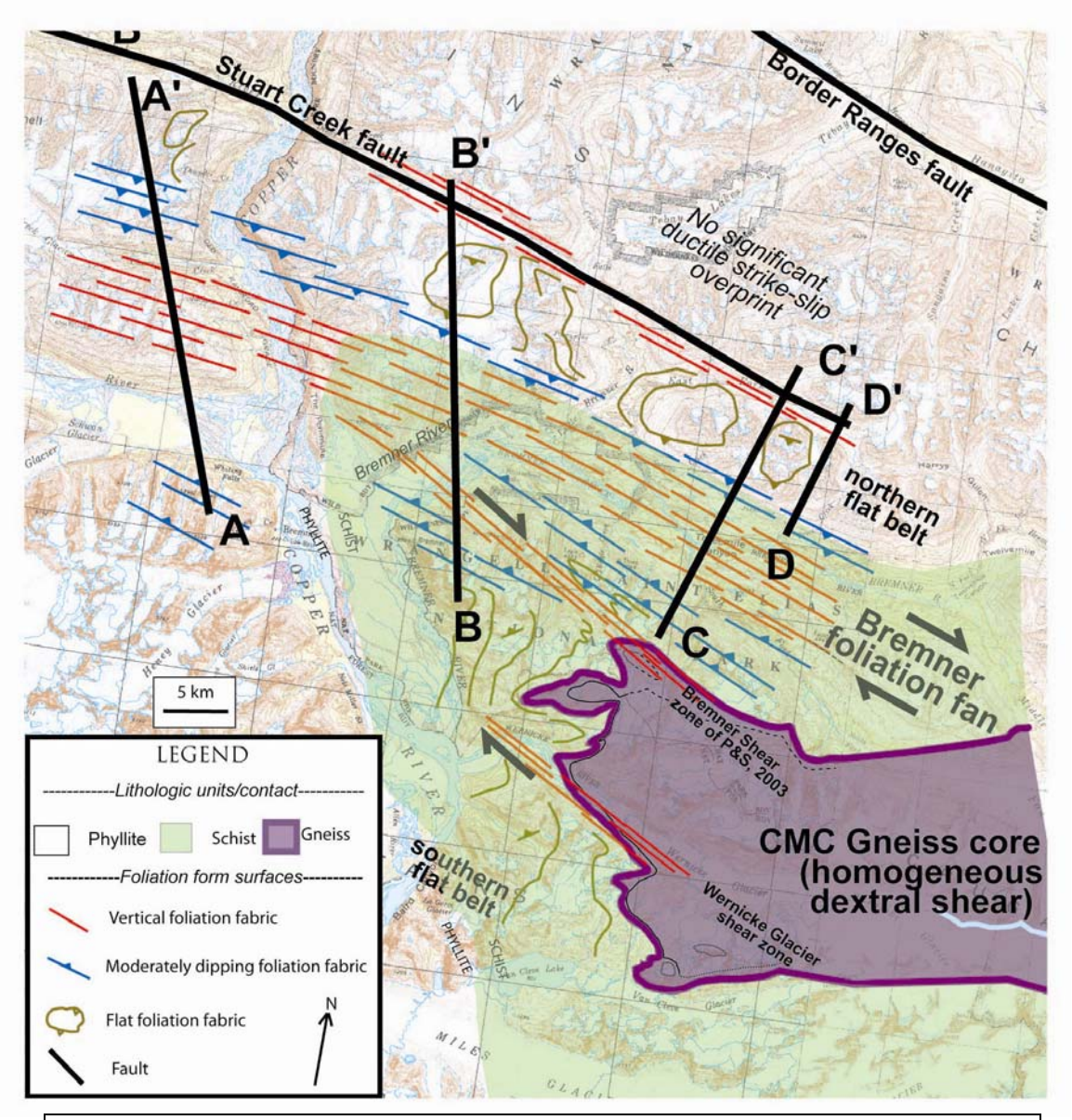


Figure 11. Generalized foliation map of the field area shown in figure 1b. Mapped foliation is broken into three domains according to steepness of dip, yielding a symmetric flower structure like geometry termed a “foliation fan.” This large-scale structure is directly adjacent to the western termination of the CMC, shown in purple and light green.

macroscopic feature in a composite set of orthographic photographs. On either side of the vertical foliation, moderate dipping foliation forms a symmetric pattern about the vertical zone. These moderately dipping bands dip toward the center of the vertical zone, forming a synformal cusp that herein is referred to as a

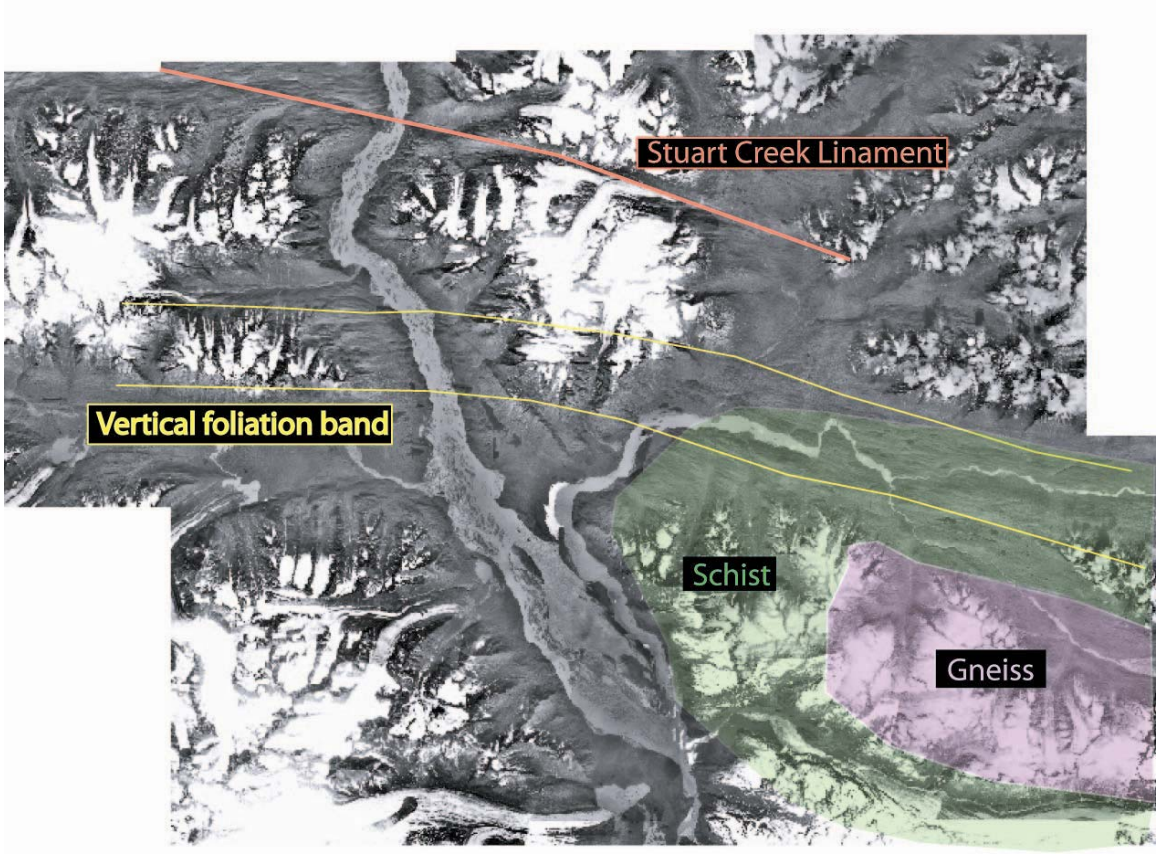


Figure 12. Othographic photo mosaic of the area shown in figure 11. Note the visible structure outlined in yellow (vertical foliation band).

"foliation fan." Two flat domains to the north and south of the moderate dip domains complete this fan shaped geometry. Figure 13 illustrates the foliation fan along multiple cross sections from figure 11. Two other vertical zones are present on the southern half of the foliation map. These zones are the Bremner and Wernicke Glacier shear zones previously described in Pavlis and Sisson (2003). Field relations clearly shows that these shear zones are $D_3$ features that are younger than the foliation fan.

The cross sections represent first ($D_1$) and second ($D_2$) phase fabrics. Layering ($S_0$) and layer parallel first phase foliation ($S_1$) are presented with

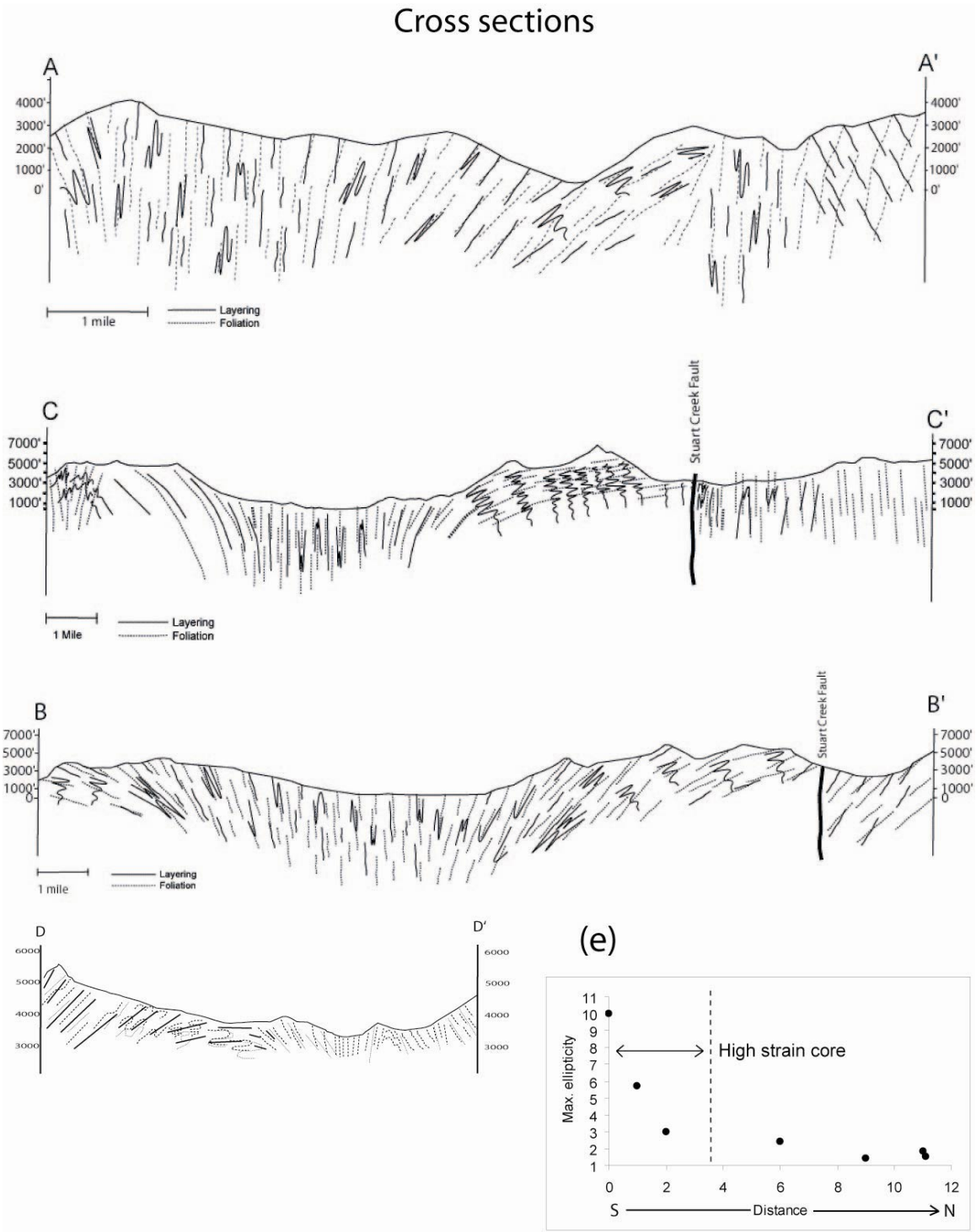


Figure 13. Cross sections from figure 11. Bold lines indicate layering and light lines indicate foliation. Foliation fan geometry best illustrated in section B. Overprint of Bremner shear zone appears in the left end of section C. (e) Plot of maximum finite strain ellipticity vs. along strike projection of sample location onto section B shows a clear correlation of vertical fabric and high strain.

heavier linework, whereas lighter weight lines show second phase ($S_2$) foliation. Accompanying cross section B-B' is locations of finite strain samples that have been projected along strike onto the section. This comparison of data sets allows description of the strain distribution across the foliation fan (Figure 13e).

Results from finite strain analysis are presented in figure 14 and table 1. Locations of samples are shown on the same area described by the foliation map along with representative oriented 3D ellipsoids. These data provide constraints for the modeling efforts presented in the remainder of this paper.

Modeling

The results from modeling incorporate modification of the attachment zone model described above. Figure 15 shows the main versions of the attachment zone model presented below immediately following output from Matlab. All figures assume model geometry similar to shear zone geometry in the CMC with a vertical EW dextral shear system transferring downward through an attachment zone.

Figure 15a is a reproduction of the Teyssier and Cruz (2004) model using the code developed in this study. While this version is just a reproduction of the model by Teyssier and Cruz (2004), it includes finite strain magnitude for each element. This feature allows for the correlation of modeling results with the finite strain measurements presented above. The colors in the background of each element indicate the magnitude of maximum ellipticity (long to short axis ratio). The dashed blue box on figure 16c (compare figures 15 & 16) shows the location

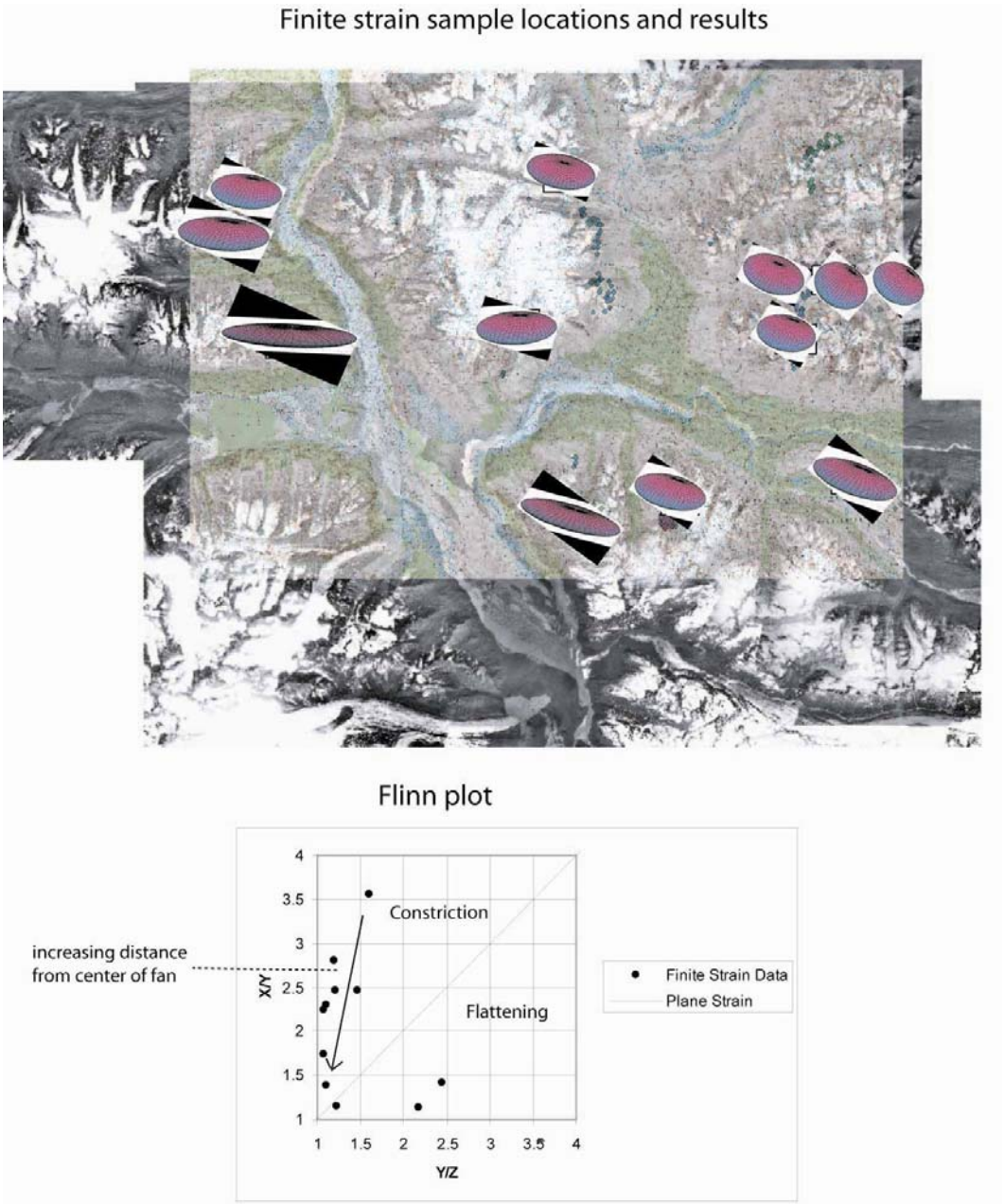


Figure 14. Summary of finite strain analysis. (top) Location of samples with respect to the field area. (bottom) Flinn diagram illustrating the dominantly constrictional character of the field area.

of the foliation pattern that inspired application of the attachment zone model to this study (Pavlis and Sisson, 2003).

Prior to obtaining the finite strain measurement in this study, the synformal foliation cusp in the dashed box seemingly predicted a foliation pattern consistent

| sample | X/Y ratio | Y/Z ratio | X/Z ratio | Long axis (Trend/Plunge) | Intermediate Axis | Short axis | Foliation (finite strain) | Foliation (field data) |
|---|---|---|---|---|---|---|---|---|
| **04APa45** | 1.15 | 1.22 | 1.403 | 162/44 | 267/11 | 9/44 N | 279/46 | |
| **04APa4** | 1.42 | 2.45 | 3.479 | 271/8 | 24/72 | 180/17 | 89/73 | 92/2 |
| **04ALO126** | 2.24 | 1.08 | 2.4192 | 290/9 | 196/21 | 40/67 | 310/23 | 286/80 |
| **04ALO84** | 2.3 | 1.1 | 2.53 | 296/3 | 28/35 | 203/55 | 113/35 | 120/85 |
| **04ALO30** | 1.13 | 2.17 | 2.4521 | 249/32 | 140/27 | 20/46 | 288/47 | 285/44 |
| **04ALO25A** | 1.74 | 1.07 | 1.8618 | 280/5 | 170/77 | 11/13 N | 280/77 | 275/45 or 275/89 |
| **04ALO24B** | 1.38 | 1.11 | 1.5318 | 264/39 | 42/43 | 155/22 | 65/78 | 265/25 |
| **04AED75** | 2.46 | 1.47 | 3.6162 | 260/50 | 14/19 | 117/34 | 26/57 | |
| **04AED57** | 3.56 | 1.6 | 5.696 | 334/10 | 75/47 | 234/42 | 144/49 | |
| **04AED41** | 2.46 | 1.21 | 2.9766 | 108/7 | 5/63 N | 108/7 | 110/64 | |
| **04ALO129** | 2.81 | 1.19 | 3.3439 | 84/3 | 353/18 | 181/72 | 91/8 | 75/83 |

Table 1. Summary of finite strain data taken from output of *3Dstrain results*. For each analyzed sample, the ratio of elliptical axes representing principle strain sections is given. The orientation of each principle axis is given in terms of long, intermediate, and short axes. Foliation of finite strain axes is reported as the plane nomal to the short axis. For comparison, the measured foliation from the sample collection site is in the far right column.

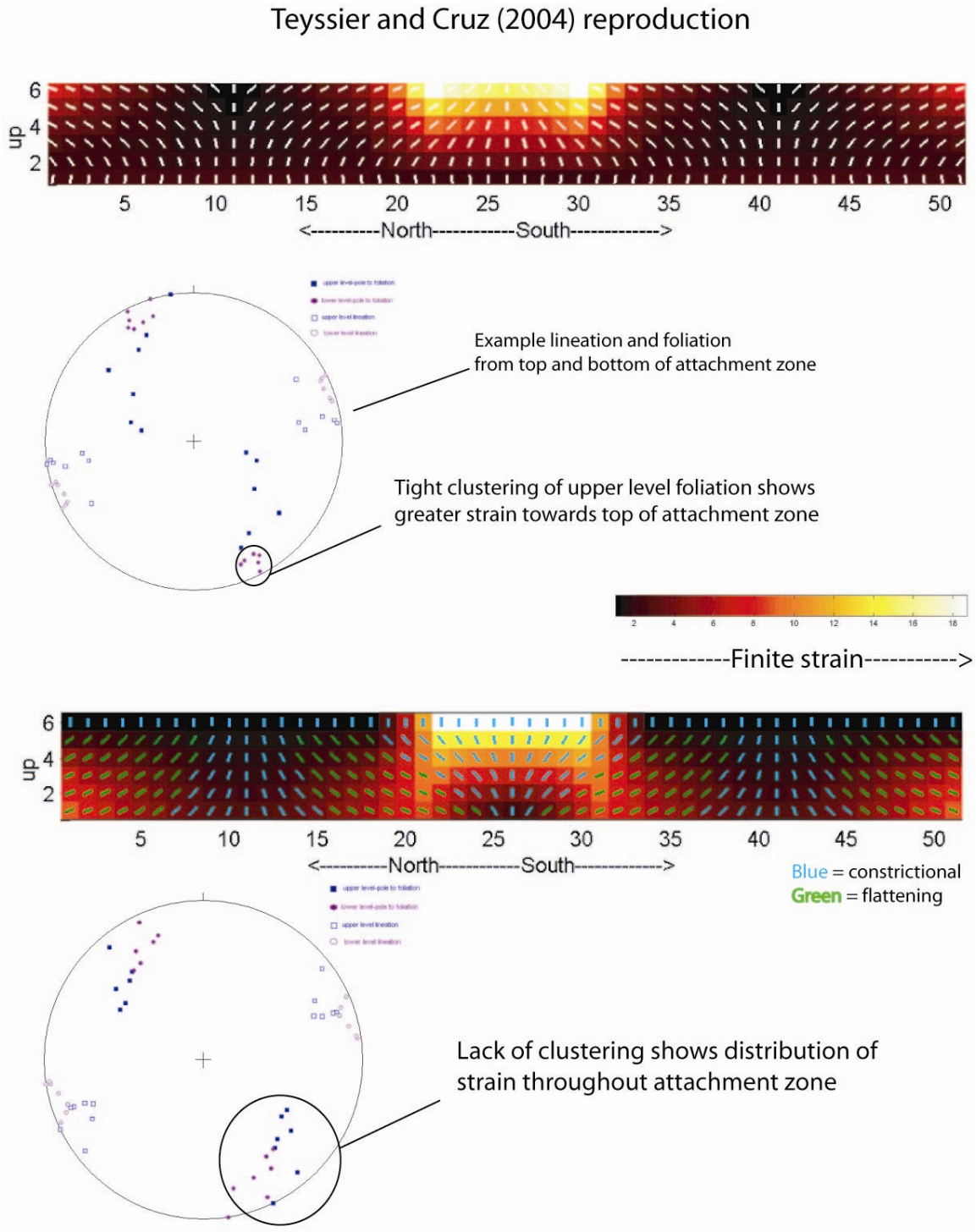


Figure 15. Attachment zone model cross sections generated in MATLAB. (top) Reproduction of model presented in Teyssier and Cruz (2004), including orientation data from the top and bottom of the attachment zone. (bottom) Analogous figure representing the best choice of attachment zone modification. This model is termed the 'inverted' attachment zone due to the inversion of boundary layers and resultant inversion of att zone geometry and strain gradients.

with the foliation fan in the western termination of the CMC. Included with the foliation geometry, opposing shear sense on either side of the foliation cusp is also predicted by the model with top west shear to the south and top to the east shear to the north. Evidence for shear sense domains were not observed in either field evidence or quartz c-axis analysis in the foliation fan (Day, personal communication). Pavlis and Sisson (2003), however, recognized scattered evidence for top-east shear during D2 in rocks directly to the south of the fan.

The fundamental observation from the new finite strain data in this study (Table 1) is that core of the foliation fan contains the highest finite strains within the foliation fan. This observation is in direct contradiction of the predications of the attachment zone model, and together with the scattered shear sense observations of Pavlis and Sisson (2003) seemingly precludes direct application of the attachment zone model to this system.

Because of this contradiction, I developed an alternative version of the attachment zone model. Figure 15b is the preferred modification of the attachment zone model, where the boundary conditions have been inverted and the blocks are allowed to deform. Alternate variations are discussed in the next subsection. The inverted attachment zone with deforming blocks allows for the most comprehensive reproduction of mapped geometry and measured finite strains. The key modification in my modeling efforts is the inversion of the model boundary layers. This change effectively relocated the position of the synformal foliation cusp.

Figures 16 and 17 include a representative block diagram illustrating the boundary condition layers above and below the attachment zone (a), a map view of

these layers (b), and a block diagram including the attachment zone accompanied by magnitude of finite strain in the background (c). These figures place the attachment zone in the context of crustal stratification. The location of the brittle-ductile transition is indicated on both models, with the transition above the entire system on the inverted model version. With a homogeneously shearing layer, the attachment zone, and the shearing blocks layer, the inverted attachment zone consists of three ductile layers. In comparison, the uppermost layer in the Teyssier and Cruz (2004) version is brittle, resulting in a more simple ductile stratification of the crust. The distinction between these two models provides a main feature to focus upon for the discussion and conclusions presented below.

An advantage of using the attachment zone model is its ability to provide foliation and lineation orientations for each element. This provides another useful tool to compare modeling results to data collected from field work. Figure 18 shows the predicted lineation directions from the upper level of the inverted attachment zone (top). This data has been rotated to account for the shallow plunge of the crustal section at the western termination of the CMC. The symmetry about the center of the model is clearly illustrated on the model stereonet. For comparison, the data presented in figure 5 are provided (lineations on left of field data). While the orientations do not match perfectly, there is general similarity amongst the two sets of data. The discrepancy

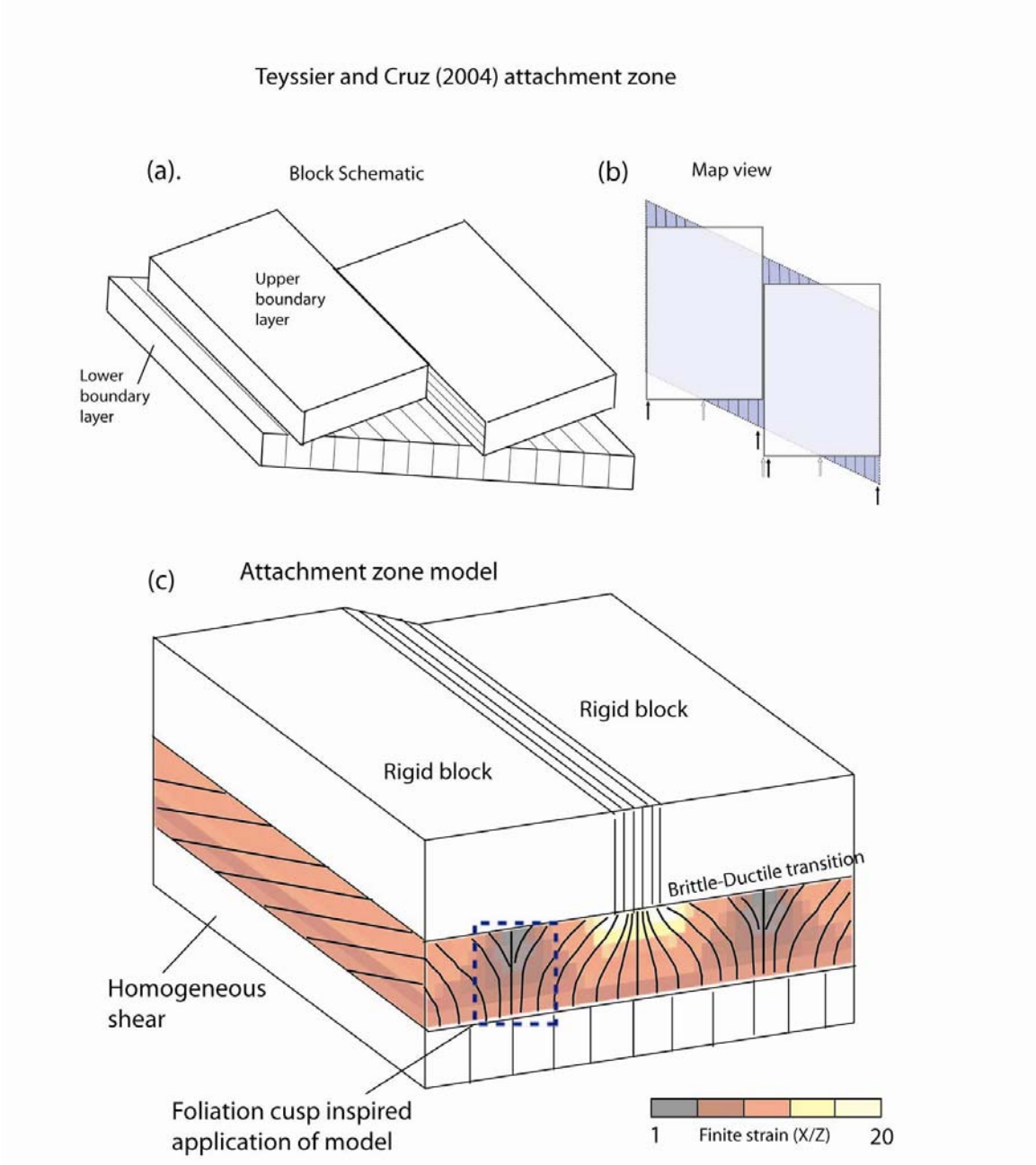


Figure 16. Summary of Teyssier and Cruz (2004) model. (a) Schematic diagram of boundary layers. (b) Map view of boundary layers, showing location of maximum and minimum differential offset amongst layers. These extrema provide locations of expected horizontal and vertical foliation, respectively. (c) Crustal column including the location of the attachment zone within the boundary layers. Foliation fan geometry outlined in dashed blue line coincided with a finite strain minimum.

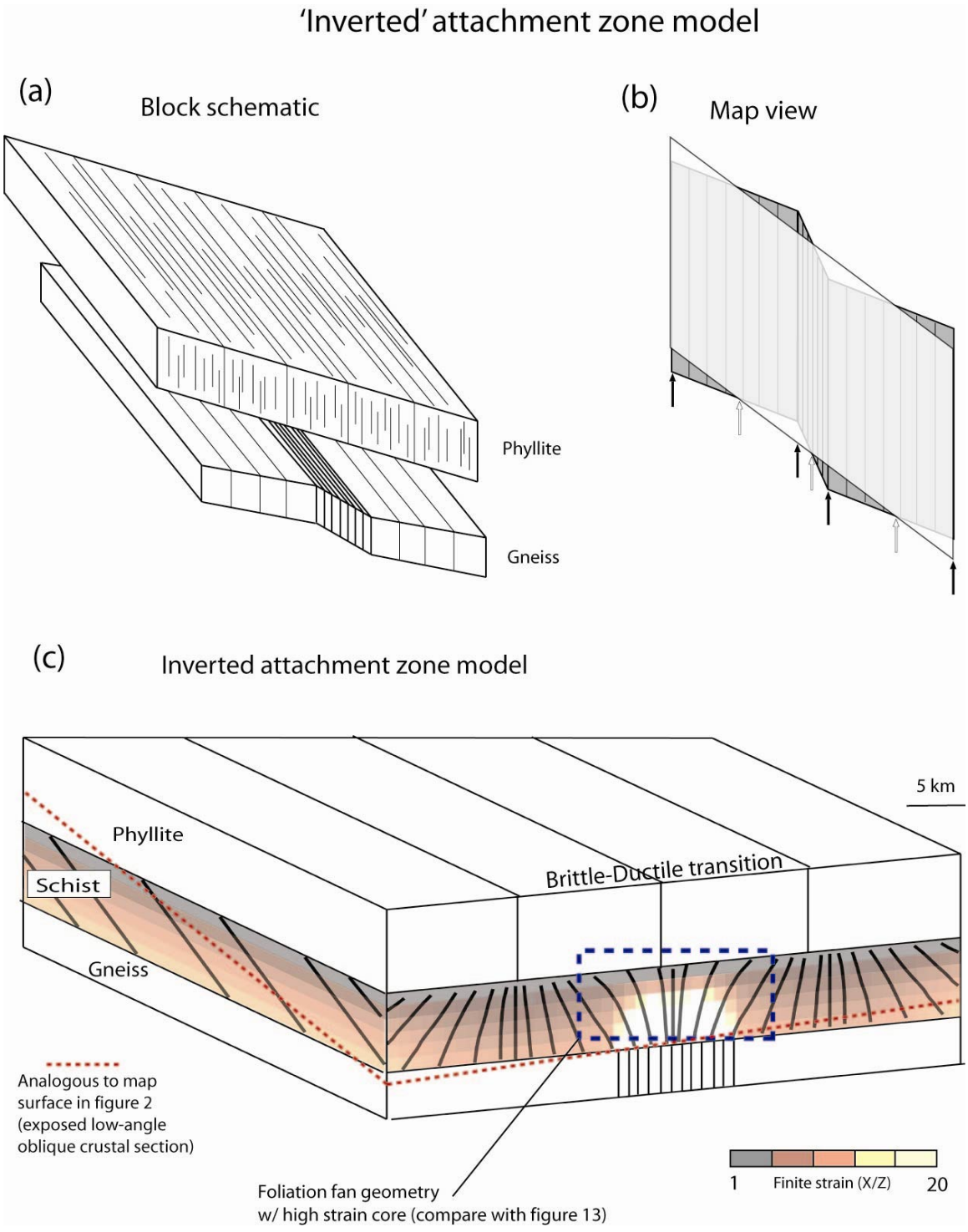


Figure 17. Summary of inverted attachment zone model. (a) Inverted boundary layers. (c) This model meets the criterion of matching structural and finite strain data. The foliation fan geometry coincides with the zone of high finite strain.

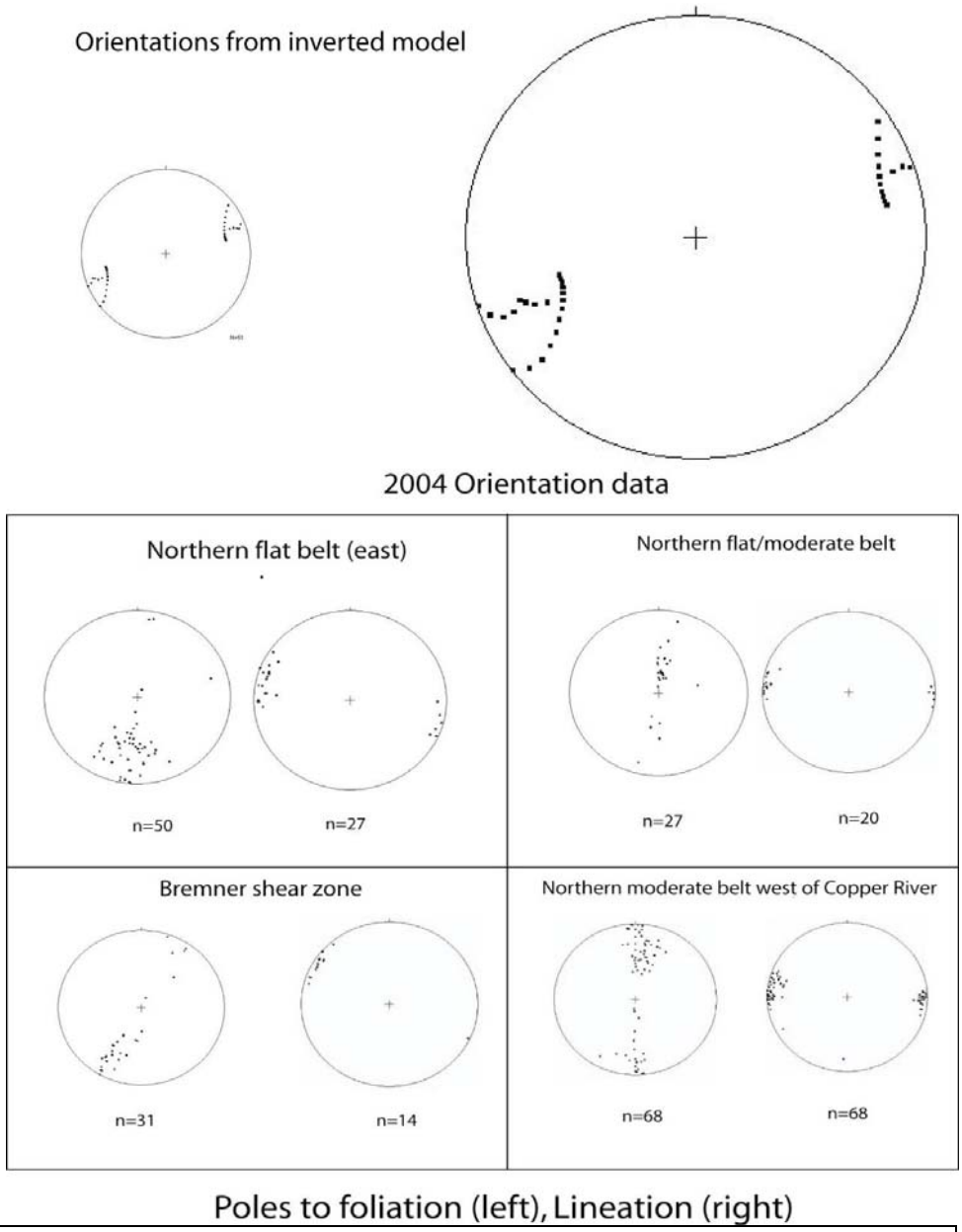


Figure 18. Comparison of foliation and lineation data from field work and modeling. (top) Representative lineation data from inverted attachment zone model has been rotated to simulate the plunge of the CMC. (bottom) Lineation data on right of each data set shows consistent E-W trends.

amongst the two can be attributed to more complex finite strain accumulation of mapped structures. Although the orientation data do not provide a perfect fit, the consistency of these data, finite strain magnitude, and foliation geometry provide a good correlation between modeling results and field based observations.

Alternate attachment models

The two models discussed above include the original attachment zone (Teyssier et al., 2002; Teyssier and Cruz, 2004) and a preferred modification developed in this research. There are however, other modifications that were tried before modeling an inverted attachment zone (Figure 19). Notable variations include a different definition of vertical strain gradients, inclusion of a third simple shear strain, and different proportions of block deformation within the inverted attachment zone.

The altered vertical strain gradient model was built with a different dispersion of the horizontal strain, $\gamma_{HS}$. The dashed curve on figure 9b shows the strain profile, plotted at a hyperbolic tangent rather than being linear with depth. The attachment zone schematic in figure 9b for this modification would have no strain at the uppermost level of the attachment zone, with the strain gradient increasing with depth as a function of the hyperbolic tangent (Figure 19a). This modification results in greater finite strain and flatter dip angles at the lower levels of the attachment zone in comparison with the Teyssier and Cruz (2004) version. This modification, however, does not help to better explain field mapping and finite strain results.

The addition of a third simple shear strain is an attempt to include the hypothesis of ductile flow in an obliquely convergent accretionary prism as described by Platt (1993, 2000). This third simple shear strain is the consequence of ductile flow sub-parallel to the convergence direction of an accretionary prism; termed “corner flow” (see Platt, 2000, Figure 2). To include

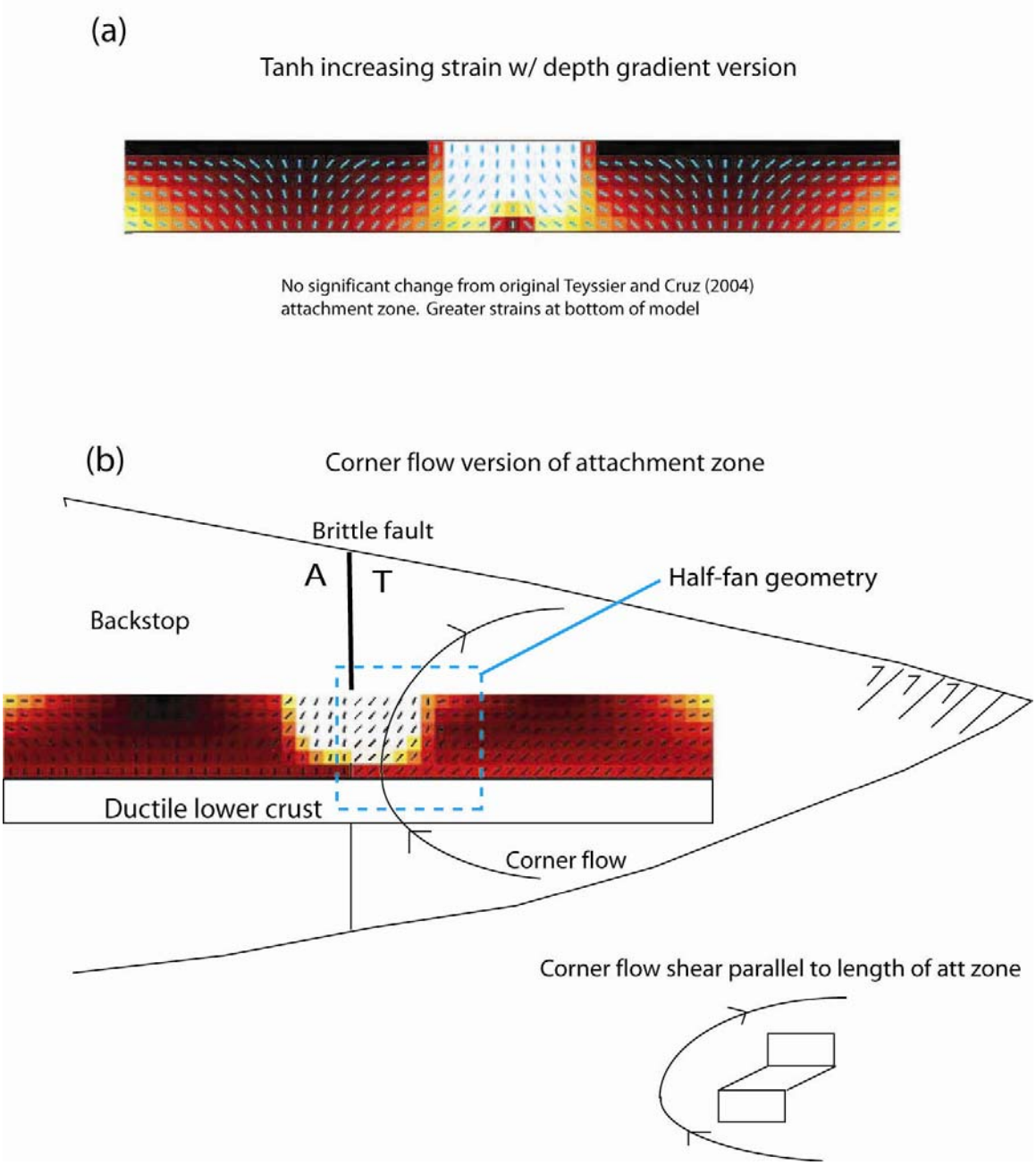


Figure 19. Failied alternative variations of the attachment zone model. (a) Result of varying the vertical strain gradient of gammaHS values does not match observational data. (b) Incorporation of oblique corner flow in the accretionary prism doesn't allow the symmetry necessary to simulate foliation fan geometry.

this strain in the attachment zone model, a third strain value is entered into the upper diagonal positions of the deformation matrix ($D_{23}$, Figure 10). The two other shear

strains described above account for motion in and out of the attachment zone plane. This third strain differs in orientation, describing shear motion parallel to the long direction of the attachment zone. By defining this corner flow, the attachment zone would be spatially fixed to the backstop of the accretionary prism (Figure 19b). The center of the attachment zone would lie below a strike-slip fault defining the contact between the backstop and accretionary wedge. Corner flow is therefore only added into the half of the attachment zone that is inside the accretionary wedge. This inclusion appropriately modifies the Teyssier and Cruz (2004) model to fit observational data where corner flow is included. However, the other half of the model does not exhibit the symmetry necessary to provide a satisfactory reproduction of the mapped foliation pattern or measured finite strain.

Lastly, differing amounts of block deformation in the inverted attachment zone model provide a range of possible models with widely variable consequences. With no block deformation, the inverted attachment zone simulates a brittle fault/shear zone motion beneath a deformable plastic layer. This crustal stratification is appropriate to describe soft sediment deformation above a basement strike-slip fault (e.g. Naylor et al., 1986), or a transform fault subducting beneath ductile crust. The latter is analogous to the left end-member on figure 20. As discussed below, this option could be valid, but poses a difficult hypothesis to test. Figure 20 shows a continuum of models illustrating the 0% block motion end member described above, to the ~100% block motion end member on the right. While this end member is not inappropriate for drawing

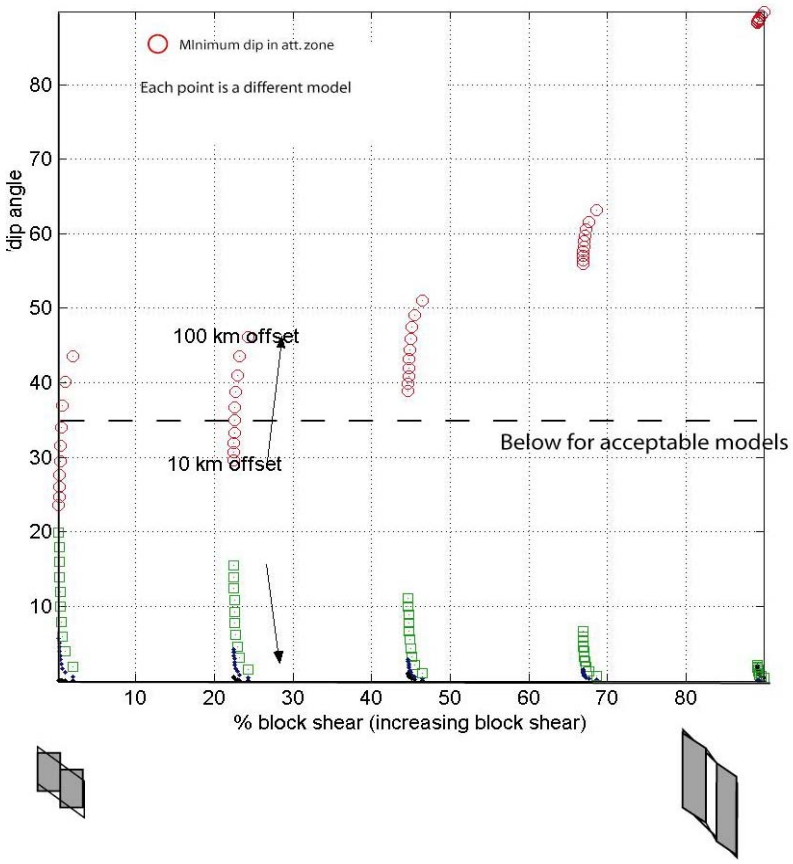


Figure 20. Explanation of shear within the boundary layer that includes shear zone. Plot of percentage of shear within blocks vs. minimum dip angle in corresponding attachment zone model. The minimum dip angle is used as a criterion to allow an maximum amount of block shear into the boundary layers. The inclusion of a maximum amount of block shear is an attempt to establish a more reasonable geologic environment for a deep crustal block.

analogies to observational data, it is instructive to explain the effect of block deformation. Greater differential motion between the upper and lower layers of the attachment zone is responsible for producing flat fabrics (due to shear on a horizontal plane). The left end member from figure 20 shows the greatest horizontal shear strain, $\gamma_{HS}$, while the right end member shows the least (compare green squares). A map view schematic is provided for each end member beneath the % block motion axis, illustrating the differential horizontal motion of each (compare gray blocks to open boxes). This continuum of % block deformation can be constrained by choosing a

confining parameter such as minimum dip of model foliation. The dashed line in figure 20 represents this parameter, establishing a pass/fail relationship with respect to a minimum dip value of 35 degrees. Each model that plots at or below that line is considered acceptable. This criterion allows for determination of an attachment zone model that includes a maximum amount of block deformation. The intersection of the minimum dip line and the 50 km offset model indicates that 25% block motion is allowable for the inverted attachment zone model and hence, my preferred model.

## Discussion

### Modeling

The attachment zone model is a purely kinematic model but its formulation (Teyssier and Cruz, 2002) is based on a fluid-mechanics model of the crust/lithosphere (Bourne et al., 1998) that assumes a simple compatibility between rigid body slip in the upper crust and distributed viscous flow in the lower crust or upper mantle. The implicit assumption in the model is a mechanical stratification from fault slip downward, through a brittle-ductile transition, into distributed flow. The model makes simple predictions that can be readily tested by field observations, and in our initial field work we were struck by similarities in the geometry of observed versus theoretical structures (e.g. Day et al., 2004). With new finite strain data (Figure 2b), however, it is clear that the predicted geometry of attachment zones is an insufficient test of the model and that finite strain information preclude the direct application of the attachment model to explain the foliation fan in the CMC.

Our alternative model can explain both the observed geometry and finite strain distribution across the foliation fan, but is counterintuitive to traditional views of the mechanical stratification of the lithosphere. Specifically, the model is an upside-down equivalent to the attachment model, but this implies a narrow shear zone at depth transitions upward through a transitional layer to a broad zone of distributed shear. We suggest three tectonic scenarios that could lead to this result:

1) upside down rheological stratification: An "upside down" flow with distributed flow overlying a ductile shear zone could have given rise to the D2 foliation fan described here. One possibility is that this flow pattern originated from a rheological stratification that occurred during D2 while the CMC was undergoing rapid heating. Under this condition deeper-seated rocks could have been deforming by crystal plastic mechanisms and shallower-level rocks were deforming by pressure solution. Since crystal plasticity generally leads to nonlinear, pseudo-plastic flow whereas pressure solution leads to linear-viscous flow (Elliot, 1973), this deformation-mechanism stratification would lead to strain localized shear zones at depth with overlying, more distributed deformation related to linear viscous flow. This may, in fact, be the case for D2 structure in the CMC with pressure solution in structurally higher level rocks to the west passing downward into crystal plastic mechanisms.

2) Subducted transform: Since the prograde metamorphism in the CMC was driven by ridge subduction, there were likely complex ridge-trench interactions that occurred in association with the ridge subduction. One possibility is the subduction of transform segments (e.g. Sisson et al., 2003), and it is conceivable this process could have helped generate the foliation fan. In this scenario, rigid blocks of oceanic crust

would have been present beneath heated pseudo-plastic crust in the overlying accretionary prism. Here, the model presented in figure 5 would be modified such that the lower level blocks are completely rigid, and separated by a discrete fault rather than a shear zone. As a result, the model foliation fan would be narrower, and the horizontal transition from vertical to flat foliation would be more abrupt. The two options above are inspired by consideration of a strike slip fault causing basement-driven deformation of a sedimentary basin (Naylor et al., 1986).

3) Counterflow in an obliquely convergent wedge: Platt (1993, 2000) developed a theory for obliquely convergent viscous wedges that provides an intriguing possibility for the origin of the observed foliation fan. This model predicts oblique counterflow within a viscous wedge with strike-slip dominated motion at depth near the "backstop" of the wedge, and subhorizontal shear at higher levels of the wedge related to counter-flow. Qualitatively this model fits many aspects of the observed foliation fan, although our initial attempts to model this interaction suggest a distinct asymmetry to foliation patterns that is not observed in CMC. The model does, however, predict local constrictional strain that is consistent with observed finite strains (e.g. Pavlis and Sisson, 2003).

Confirmation of one or a combination of these scenarios would provide significant insight into local and regional crustal deformation. In the case of the attachment zone model, there are important implications for the operating deformation mechanisms and associated rheology. In the case of "upside down" rheologic stratification those predictions are quite different, and may reflect important distinctions in the prograde D2 path vs. syn-peak temperature deformation (D3) in the CMC. If this were confirmed,

this thermal distinction could ultimately have fundamental implications for the mechanical behavior of the crust under different thermal regimes.

While the inverted attachment model provides a reasonable fit to our observations, the oblique wedge model of Platt does provide an attractive alternative. A wedge model is consistent with the development of the complex within an accretionary complex and considers wholesale motion of the crust, but this model has a different significance. In particular, to fit our observations this model would require a distinct temporal evolution with successive structural overprints representing material paths through an accretionary complex. Similar paths have been suggested elsewhere (Koons et al., 2004) but not in the context of ridge subduction.

Regional geology

Structures corresponding to a minimum of three deformational conditions have been identified in the study areas shown in figure 11. Layer parallel cleavage can confidently be associated with convergence within the accretionary prism ($D_1$). The two other deformational events are marked by the presence of the entire foliation fan and the Bremner and Wernicke Glacier shear zones, respectively.

Pavlis and Sisson (2003) account for the formation of the Bremner shear zone during $D_3$ deformation. The data presented in the lower left corner of figure 5 is from the southern edge of the BSZ. By comparing these data to orientations from the other camps within the foliation fan, it is clear that BSZ deformation is from a younger generation. Therefore, the formation of the foliation fan should be placed within the $D_2$ period of deformation.

$D_2$ deformation is closely linked to active ridge subduction (Pavlis and Sisson, 1995). During this time, the results of this work suggest the presence of ductile flow within the middle to lower crust. Given the anomalously high thermal gradient associated with the presence of an adjacent slab window, intense ductile deformation is indeed expected. Further development of attachment zone model variations will provide insight into the role of ductile flow during $D_2$ deformation.

## Conclusions

The inverted attachment zone model provides the simplest explanation for observed relationships in the CMC. The kinematic system indicated by the model suggests either a switch in rheologic stratification during prograde metamorphism associated with ridge subduction, or a system complicated by a subducting transform during ridge subduction. Alternatively, the system is neither of these alternatives and formed by flow within the accretionary wedge during ridge subduction, an alternative that requires further analysis. In any case, the CMC represents a spectacular natural exposure where mid-crustal flow processes ranging from rheologic effects of deformation mechanism changes to basic flow patterns may eventually be distinguishable.

## References


Atwater, T., 1970, Implications of plate tectonics for the Cenozoic tectonic evolution of western North America, *GSA Bulletin*, v. 81, pp. 3513-3535

Bol, A. J., 1993, Overprint magnetizations in support of northward displacement of the Chugach-Prince William Terrane, Alaska, *Journal of Geophysical Research*, v. 98, Issue B12, pp. 22,389-22,400

Bourne, S. J., England, P. C., Parsons, B., 1998, The motion of crustal blocks driven by flow of the lower lithosphere and implications for slip rates of continental strike-slip faults, *Nature*, v. 391, Issue 6668, pp. 655-659

Bradley, D. C., Kusky, T .M., Haeussler, P. J., Goldfarb, R. J., Miller, M. L., Dumoulin, J. A., Nelson, S. W., Karl, S. M., 2003, *in* Geology of a transpressional orogen developed during ridge-trench interaction along the North Pacific margin. Sisson, V. B., Roeske, S. M., Pavlis, T. L. [eds.], GSA special paper 371, pp. 19-49

Clark, S. H. B., 1981, Guide to the bedrock geology along the Seward Highway, north of Turnagain Arm, *Alaska Geological Society Publication*, v. 1, 36 p.

Cowan, D.S., Brandon, M. T., 1981, Contrasting facies in upper Mesozoic strata of Pacific Northwest, *AAPG Bulletin*, v. 65, pp. 913-914

Day, E., Pavlis, T. L., O'Driscoll, L. J., 2004, A down-plunge section of a Paleogene strike-slip shear zone from low-grade phyllite to high-grade gneiss in the Chugach metamorphic complex, Southern Alaska, *Abstracts with Programs-GSA*, v. 36, issue 5, pp. 254

Elliott, D., 1973, Diffusion flow laws in metamorphic rocks, *GSA Bulletin*, v. 84, pp. 2645-2664

Farmer, G. L.., Ayuso, R., Plafker, G., 1993, A Coast Mountains provenance for the Valdez and Orca groups, Southern Alaska, based on Nd, SR and Pb isotopic evidence, *Earth and Planetary Science Letters*, v. 116, pp. 9-21

Fossen, H., Tikoff, B., 1993, The deformation matrix for simultaneous simple shearing, pure shearing and volume change, and its application to transpression-transtension tectonics, *Journal of Structural Geology*, v. 15, pp. 413-422

Harris, N. R., Sisson, V. B., Wright, J., Pavlis, T. L., 1996, Evidence for Eocene mafic underplating during forearc intrusive activity, eastern Chugach Mountains, Alaska, *Geology*, v. 24, pp. 263-266

Hudson, T., Plafker, G., 1982, Paleogene metamorphism of an accretionary flysch terrane, eastern Gulf of Alaska, *GSA Bulletin*, v. 93, issue 12, pp. 1280-1290

Koons, P. O., Upton, P., Johnson, S., Jessel, M., 2004, Model strain and model fabric development in 3D oblique orogens, *GSA Abstracts with Programs*, v. 36, p. 437

Naylor, M. A., Mandl, G, Sijpesteijn, C. H. K., 1986, Fault geometries in basement-induced wrench faulting under different initial stress states, *Journal of Structural Geology*, v. 8, pp. 737-752

Nilsen, T. H., Zuffa, G. G., 1982, The Chugach Terrane, a Cretaceous trench-fill deposit, southern Alaska, *in* Trench-Forearc geology; sedimentation and tectonics on modern and ancient active plate margins, conference. Leggett, J. K. [editor], pp. 213-227

Pavlis, T. L., Sisson, V. B., 1995, Structural history of the Chugach metamorphic complex in the Tana River region, eastern Alaska; a record of Eocene ridge subduction, *GSA Bulletin*, v. 107, issue 11, pp. 1333-1355

Pavlis, T. L., Sisson, V. B., 2003, Development of a subhorizontal decoupling horizon in a transpressional system, Chugach metamorphic complex, Alaska; evidence for rheological stratification of the crust, *in* Geology of a transpressional orogen developed during ridge-trench interaction along the North Pacific margin. Sisson, V. B., Roeske, S. M., Pavlis, T. L. [eds.], GSA special paper 371, pp. 191-216

Pavlis, T. L., Marty, K., Sisson, V. B., 2003, Constrictional flow within the Eocene forearc in southern Alaska; an effect of dextral shear during subduction, *in* Geology of a transpressional orogen developed during ridge-trench interaction along the North Pacific margin. Sisson, V. B., Roeske, S. M., Pavlis, T. L. [eds.], GSA special paper 371, pp. 171-190

Plafker, G., Moore, J. C., Winkler, G. R., 1994, Geology of the Southern Alaska margin, *in* DNAG: The Geology of Alaska, Plafker, G., Berg, H. C., [eds.], v. G-1, pp. 389-449

Platt, J. P., 1993, Mechanics of oblique convergence, *Journal of Geophysical Research*, v. 98, issue B9, pp. 16,239-16,256

Platt, J. P., 2000, Calibrating the bulk rheology of active obliquely convergent thrust belts and forearc wedges from surface profiles and velocity distributions, *Tectonics*, v. 19, issue 3, pp. 529-548

Sample, J. C., Fisher, D. M., 1986, Duplex accretion and underplating in an ancient accretionary complex, Kodiak Islands, Alaska, *Geology (Boulder)*, v. 14, issue 2, pp. 160-163

Sisson, V. B., Hollister, L. S., Onstott, T. C., 1989, Petrologic and age constraints on the origin of a low-pressure/high-temperature metamorphic complex, southern Alaska, *Journal of Geophysical Research*, v. 94, issue B3, pp. 4392-4410

Sisson, V. B., Pavlis, T. L., 1993, Geologic consequences of plate reorganization; an example from the Eocene Southern Alaska fore arc, *Geology (Boulder)*, v. 21, issue 10, pp. 913-916

Sisson, V. B., Poole, A. R., Harris, N. R., Burner, H. C., Pavlis, T. L., Copeland, P., Donelick, R. A., McLelland, W. C., 2003, Geochemical and geochronologic constraints for genesis of a tonalite-trondhjemite suite and associated mafic intrusive rocks in the eastern Chugach Mountains, Alaska; a record of ridge-transform subduction, *in* Geology of a transpressional orogen developed during ridge-trench interaction along the North Pacific margin. Sisson, V. B., Roeske, S. M., Pavlis, T. L. [eds.], GSA special paper 371, pp. 293-326

Teyssier, C., Tikoff, B., Weber, J., 2002, Attachment between brittle and ductile crust at wrenching plate boundaries, *European Geophysical Union, Stephan Mueller Special Publication*, v. 1, pp. 75-91

Teyssier, C., Cruz, L., 2004, Strain gradients in transpressional to transtensional attachment zones, *in* Vertical coupling and decoupling in the lithosphere. Grocott, J., McCaffrey, K. J. W., Taylor, G., Tikoff, B. [eds.]

Tikoff, B., Fossen, H., 1993, Simultaneous pure and simple shear: the unifying deformation matrix, *Tectonophysics*, v. 217, pp. 267-283

Tysdal, R. G., Plafker, G., 1978, Age and continuity of the Valdez Group, southern Alaska, *in* Changes in stratigraphic nomenclature by the U. S. Geological Survey, 1977. Sohl, N. F.; Wright, W. B., pp. 120-124

Umhoefer, P., 1987, Northward translation of ‘Baja British Columbia’ along the Late Cretaceous to Paleocene margin of western North America, *Tectonics*, v. 6, pp. 377-394

**Appendix**

Presented below are three programs that (1) establish the geometry and strain quantities of the attachment zone (2) calculate the finite strain ellipsoid for each element in the model and (3) display finite strain magnitude on the attachment zone cross section.

**********THIS IS AN EXAMPLE OF A PROGRAM THAT ESTABLISHES THE GEOMETRY AND STRAIN VALUES TO BE INPUT INTO THE DEFORMATION MATRIX CALCULATIONS**********

**********START**********

```
close all

%  for k=1:10:100
%      offset=k;
%multiple defines offset amount interval
DSD=.1;  %DSD=distributed shear distance, near zero simulates rigid blocks
B1E=0; B1S=0; B1N=22.5;  %initial parameters of block 1,
B1domain=B1E:(DSD-B1E)/22:DSD; %make 23 intervals
B1output=(B1N/DSD).*B1domain;
hold on

offset=50; %X=offset amount
B2S=27.5; B2E=offset+DSD;      %, B2S defines Shear Zone width, Block2 has same
DSD
SZdomain=DSD:(B2E-DSD)/4:B2E;  %make 5 intervals
m=(B2S-B1N)/(B2E-DSD); b=B1N-m.*DSD;
SZoutput=m.*SZdomain+b;

B2N=50; B2Eoffset=B2E+DSD;      %block2 has same DSD as block 1
B2domain=B2E:(B2Eoffset-B2E)/22:B2Eoffset; %make 23 intervals
m=(B2N-B2S)/DSD;  b=B2S-m.*B2E;
B2output=m.*B2domain+b;

uppercrustposition=[B1domain SZdomain B2domain];   %place all lower ductile crust
values into one matrix

%define upper ductile crust position in each of the 3 domains defined above
```

```
m=(B2Eoffset+B2E-DSD)/(B2N+B2S-B1N); b=(DSD/2)-m.*(B1N/2);

LC1range=B1S:(B1N-B1S)/22:B1N;
LC1=m.*LC1range+b; %each domain shares the same equation, they are broken up to
correspond with lower crust positions
LC2range=B1N:(B2S-B1N)/4:B2S;
LC2=m.*LC2range+b;
LC3range=B2S:(B2N-B2S)/22:B2N;
LC3=m.*LC3range+b;

lowercrustposition=[LC1 LC2 LC3];                %place all upper ductile crust values into
one matrix

attzonethickness=6;%(B1N-B1S)./pi;   %Bourne et al. (1996?)
gammaHSmax=(lowercrustposition-uppercrustposition)./attzonethickness;  %defined so
sign of shear is correct

SZpsi=-offset/(B2S-B1N), Blockpsi=-DSD/(B1N-B1S)  %calculate shear strain values
SZ_Blockratio=SZpsi/Blockpsi;

LCshearstrain=-offset/((B2N+B2S)/2-(B1N/2));   %calculate and assign upper crust
shear strain values
lowercruststrain=ones(size(gammaHSmax)).*LCshearstrain;

SZstrain=zeros(size(gammaHSmax));

SZstrain(1,21)=.25*SZpsi; SZstrain(1,22)=.5*SZpsi; SZstrain(1,23)=.75*SZpsi;
SZstrain(1,24)=SZpsi;...
   SZstrain(1,25)=SZpsi; SZstrain(1,26)=SZpsi; SZstrain(1,27)=SZpsi;
SZstrain(1,28)=SZpsi;...
   SZstrain(1,29)=.75*SZpsi; SZstrain(1,30)=.5*SZpsi; SZstrain(1,31)=.25*SZpsi;

Strainvalues=[SZ_Blockratio max(gammaHSmax) LCshearstrain SZpsi];

%assume a linear decrease of gHS w/ depth, the opposite for gWL and gSZ
vertgradHS=1:-1/5:0;
gammaHS=vertgradHS'*gammaHSmax;     %linear decrease of gHS with depth
gammaWSZ=vertgradHS'*SZstrain;     %""    ""              ""       ""
vertgradWlower=0:1/5:1;
gammaWlower=vertgradWlower'*lowercruststrain;       %linear increase of gHS with
depth
gammaW=gammaWlower+gammaWSZ;

%build a corner flow matrix
% gammaCF=zeros(size(gammaW));
% for n = 26:51
```

```
%     gammaCF(:,n)=1
% end

%finish for loop that extracts strain values
PSIsummary=[offset LCshearstrain max(gammaHS(1,:)) SZpsi];
figure(1)
plot(offset, abs(LCshearstrain), 'k.', offset, abs(Strainvalues(1,2)), 'b*', offset,
abs(SZpsi), 'rx')
xlabel('offset of shear zone')
ylabel('shear strain/max ellipticity')
title('Summary of shear strains')
grid on


%figure
% plot(B1domain, B1output, 'g', SZdomain, SZoutput, 'g', B2domain, B2output, 'g',...
%      LC1, LC1range,'k', LC2, LC2range, 'k', LC3, LC3range, 'k')

% figure(1)
% plot(offset , log(max(XZratiodisplay(1,:))), 'g.')
% end
% legend('Lower crust shear strain', 'detachment strain', 'SZ strain', 'Log(X/Z)',2)

*******************************END************************************


******THIS PROGRAM CALLS THE RESULTS FROM THE ABOVE PROGRAM.  EACH
ELEMENT OF THE ATTACHMENT ZONE HAS A CALCULATION OF PRINCIPLE
AXES PERFORMED VIA THE DEFORMATION MATRIX.  AFTER CALCULATION,
THE PROJECTION OF THE SHORT AXIS ONTO THE ATTACHMENT ZONE CROSS
SECTION IS PLOTTED AS SHORT LINES THAT REPRESENT FOLIATION.  THE
MAGNITUDE OF STRAIN IS PLOTTED IN THE BACKGROUND OF EACH
ELEMENT.**********************************


*******************************START**********************************

%enter appropriate model name here

%TandC04
%TANHdown
defblocks

%colordef black

Longaxistrend=zeros(size(gammaW));
```

```
Longaxisplunge=zeros(size(Longaxistrend));
RHRfoliationstrike=zeros(size(Longaxistrend));
foliationdip=zeros(size(Longaxistrend));
XZratiodisplay=zeros(size(Longaxistrend));
XY=zeros(size(Longaxistrend));
YZ=zeros(size(Longaxistrend));
figure, hold on
for z=1:1:6
   for y=1:1:51
      D=[1 gammaW(z,y) gammaHS(z,y); 0 1 0; 0 0 1];   %make this a generic file, only
use gammaW and HS
      Dvals=[gammaW(z,y) gammaHS(z,y)];

      symmprep=D*D';
      [v, eigvals]=eig(symmprep);

      valign=[v(:,3) v(:,2) v(:,1)];          %place eigenvectors in conventional positions
(a11, a12, a13; a21,...)
      dircos=acos(valign).*(180/pi);

      %calculate flinn parameters
      XY(z,y)=sqrt(eigvals(3,3)/eigvals(2,2));
      YZ(z,y)=sqrt(eigvals(2,2)/eigvals(1,1));
      XZratio(z,y)=XY(z,y)*YZ(z,y);
      XZratiodisplay(z,y)=XZratio(z,y);

      %calculate lineation trend&plunge and foliation strike(RHR)&dip

     %Produces a DOWNPLUNGE trend
     if valign(3,1)>=0
        if valign(1,1)>=0
           trend=180-dircos(2,1);
        end
        if valign(1,1)<0
           trend=dircos(2,1)+180;
        end
     end
     if valign(3,1)<0
        if valign(1,1)>=0
           trend=360-dircos(2,1);
        end
        if valign(1,1)<0
           trend=dircos(2,1);
        end
     end
```

```
%Produces plunge associated with above trend
if valign(3,1)<=0
   plunge=dircos(3,1)-90;
end
if valign(3,1)>0
   plunge=90-dircos(3,1);
end

%Produces strike of foliation according to right hand rule (RHR)
if valign(3,3)>=0
   if valign(2,3)<=0
      RHRstrike=dircos(2,3)+90;
   end
   if valign(2,3)>0
      RHRstrike=(360-dircos(2,3))+90;
   end
end
if valign(3,3)<0
   if valign(2,3)<=0
      RHRstrike=dircos(2,3)-90;
   end
   if valign(2,3)>0
      RHRstrike=270-dircos(2,3);
   end
end

 %Produces dip associated with above strike (dip direction implied in strike)
if valign(3,3)>=0
   dip=dircos(3,3);
end
if valign(3,3)<0
   dip=180-dircos(3,3);
end

%this proviso makes sure strike isn't greater than 360
if RHRstrike>360
   RHRstrike=RHRstrike-360;
end
%this proviso makes sure strike isn't negative
if RHRstrike<0
   RHRstrike=RHRstrike+360
end

%place calculated orientations into separate matrices
Longaxistrend(z,y)=trend;
Longaxisplunge(z,y)=plunge;
```

```
RHRfoliationstrike(z,y)=RHRstrike;
foliationdip(z,y)=dip;

 %plot small line elements at each point in cross section (scaled to arbitrary
domain)
 if  270<RHRfoliationstrike(z,y)<361
 elseif 0<RHRfoliationstrike(z,y)<91
    if foliationdip(z,y)<45
       b=(7-z)-(-1.*(valign(2,3)/valign(3,3))).*y;
       y_domain=y-.25:.5:y+.25;
       z_output=(-1.*(valign(2,3)/valign(3,3))).*y_domain+b;
       if XY(z,y)-YZ(z,y)<0;          %plot Flinn parameters with different patterns
          plot(y_domain, z_output, 'c', 'Linewidth', 1.5), hold on
       elseif XY(z,y)-YZ(z,y)>0
          plot(y_domain, z_output, 'c', 'Linewidth', 1.5)
       elseif XY(z,y)-YZ(z,y)==0
          plot(y_domain, z_output, 'c', 'Linewidth', 1.5)
       end
    end
    if foliationdip(z,y)>45
      c=y-(-1.*(valign(3,3)/valign(2,3))).*(7-z);
      z_domain=(7-z)-.25:.05:(7-z)+.25;
      y_output=(-1.*(valign(3,3)/valign(2,3))).*z_domain+c;
      if XY(z,y)-YZ(z,y)<0;          %plot Flinn parameters with different patterns
        plot(y_output, z_domain, 'c', 'Linewidth', 1.5), hold on
   elseif XY(z,y)-YZ(z,y)>0
        plot(y_output, z_domain, 'c', 'Linewidth', 1.5)
   elseif XY(z,y)-YZ(z,y)==0
        plot(y_output, z_domain, 'c', 'Linewidth', 1.5)
     end
   end
    if foliationdip(z,y)>=90
      z_domain=(7-z)-.25:.05:(7-z)+.25;
      y_output=0.*z_domain+y;
      plot(y_output, z_domain)
   end
end

 if  91<RHRfoliationstrike(z,y)<270
    if foliationdip(z,y)<45
       d=(7-z)-(-1.*(valign(2,3)/valign(3,3))).*y;
       y_domain=y-.25:.5:y+.25;
       z_output=(-1.*(valign(2,3)/valign(3,3))).*y_domain+d;
       if XY(z,y)-YZ(z,y)<0;          %plot Flinn parameters with different patterns
          plot(y_domain, z_output, 'c', 'Linewidth', 1.5), hold on
       elseif XY(z,y)-YZ(z,y)>0
```

```
            plot(y_domain, z_output, 'c', 'Linewidth', 1.5)
          elseif XY(z,y)-YZ(z,y)==0
            plot(y_domain, z_output, 'c', 'Linewidth', 1.5)
          end
        end
        if foliationdip(z,y)>45
          f=y-(-1.*(valign(3,3)/valign(2,3))).*(7-z);
          z_domain=(7-z)-.25:.05:(7-z)+.25;
          y_output=(-1.*(valign(3,3)/valign(2,3))).*z_domain+f;
          if XY(z,y)-YZ(z,y)<0;          %plot Flinn parameters with different patterns
            plot(y_output, z_domain, 'c', 'Linewidth', 1.5), hold on
        elseif XY(z,y)-YZ(z,y)>0
            plot(y_output, z_domain, 'c', 'Linewidth', 1.5)
        elseif XY(z,y)-YZ(z,y)==0
            plot(y_output, z_domain, 'c', 'Linewidth', 1.5)
          end
      end
      end
  end
end

Longaxistrend(z,y)=trend;
Longaxisplunge(z,y)=plunge;
RHRfoliationstrike(z,y)=RHRstrike;
foliationdip(z,y)=dip;

%Xsectionstrainbackgroundupper       %chooses which layer will define strain scale
Xsectionstrainbackgroundlower

 axis image%([-1 52 0 7])
 xlabel('<----------North------------South------------>')
 ylabel('up')
% Longaxistrend, Longaxisplunge
% Shortaxistrend, Shortaxisplunge
% XZratiodisplay

%Flinnplot
%reporients
%repFlinn
%stereoplotnew
%close(2)

*******************************END*******************************

***THIS LAST PROGRAM PLOTS THE FINITE STRAN MAGNITUDE BEHIND THE
FOLIATION TRAJECTORY FOR EACH ELEMENT*******************
```

**********START**********

```
colormap(hot)%colormap(jet)
for z=1:1:6
   for y=1:1:51
      X=[y-.5 y+.5 y+.5 y-.5]';
      Y=7*ones(size(X))-[z-.5 z-.5 z+.5 z+.5]';
      caxis([1 20]);
      C=XZratiodisplay(z,y)*ones(size(X));
      fill(X,Y,C)
      hold on
   end
end
%colorbar('horiz')
```

**********END**********

**Vita**

Leland James O'Driscoll was born October 21, 1980 in Lone Pine, CA to his parents Lee James O'Driscoll and Melodee Jean Sewell. He was raised in McKineyville, CA and graduated from McKinleyville High School (1998) and Humboldt State University (2003). Leland is currently living in Eugene, OR, working towards a Ph.D. in geodynamics under Dr. Eugene Humphreys at the University of Oregon. He has aspirations of becoming a professional geologist and disc golfer.